Shear Variation at the Ice-Till Interface Changes the Spatial Distribution of Till Porosity and Meltwater Drainage

Indraneel Kasmalkar[1], Anders Damsgaard[2], Liran Goren[3], Jenny Suckale[1,4,5]

[1]Institute for Computational and Mathematical Engineering, Stanford University, Stanford, California
[2]Department of Geoscience, Aarhus University, Aarhus, Denmark
[3]Department of Earth and Environmental Sciences, Ben-Gurion University of the Negev, Beer-Sheva, Israel
[4]Department of Geophysics, Stanford University, Stanford, California
[5]Department of Civil and Environmental Engineering, Stanford University, Stanford, California

Key Points:

- Large shear gradients at the ice-till interface create a narrow zone of elevated porosity in till.
- The porosity of granular beds increases with shear strain rate even for subglacial strain rates.
- Pore pressure equilibrates rapidly at the grain scale during critical state shear.

Corresponding author: Indraneel Kasmalkar, `ineel@alumni.stanford.edu`

This article has been accepted for publication and undergone full peer review but has not been through the copyediting, typesetting, pagination and proofreading process, which may lead to differences between this version and the Version of Record. Please cite this article as doi: 10.1029/2021JF006460.

Abstract

Many subglacial environments consist of a fine-grained, deformable sediment bed, known as till, hosting an active hydrological system that routes meltwater. Observations show that the till undergoes substantial shear deformation as a result of the motion of the overlying ice. The deformation of the till, coupled with the dynamics of the hydrological system, is further affected by the substantial strain rate variability in subglacial conditions resulting from spatial heterogeneity at the bed. However, it is not clear if the relatively low magnitudes of strain rates affect the bed structure or its hydrology. We study how laterally varying shear along the ice-bed interface alters sediment porosity and affects the flux of meltwater through the pore spaces. We use a discrete element model consisting of a collection of spherical, elasto-frictional grains with water-saturated pore spaces to simulate the deformation of the granular bed. Our results show that a deforming granular layer exhibits substantial spatial variability in porosity in the pseudo-static shear regime, where shear strain rates are relatively low. In particular, laterally varying shear at the shearing interface creates a narrow zone of elevated porosity which has increased susceptibility to plastic failure. Despite the changes in porosity, our analysis suggests that the pore pressure equilibrates near-instantaneously relative to the deformation at critical state, inhibiting potential strain rate dependence of the deformation caused by bed hardening or weakening resulting from pore pressure changes. We relate shear variation to porosity evolution and drainage element formation in actively deforming subglacial tills.

Plain Language Summary

The ice at the base of certain glaciers moves over soft sediments that route meltwater through the pore spaces in between the sediment grains. The ice shears the sediment, but it is not clear if this slow shearing is capable of changing the structure or volume of the pore space, or the path of the meltwater that flows through the sediment. To study the relations between the shearing of the sediment and the changes in its pore space, we use computer simulations that portray the sediment as a collection of closely packed spherical grains, where the pores are filled with meltwater. To shear the simulated sediment, the grains at the top are pushed with fixed speeds in the horizontal direction. Despite the slow shear, which is generally thought of as having no effect on pore space, our results show that shearing changes the sizes of the pores in between the grains, where large pores are formed near the top of the sediment layer. If the grains at the top are pushed with uneven speeds, then the largest pores are formed in the areas where grain speeds vary the most. We show that the exchange of meltwater between neighboring pores is faster than the movement of the grains, indicating that the meltwater can adjust quickly to changing pore space.

1 Introduction

Large portions of the two ice sheets, Antarctica and Greenland, are underlain by soft, deformable sediment, known as till (Blankenship et al., 1986; Alley et al., 1987; Evans et al., 2006; Christianson et al., 2014; Lindeque et al., 2016). The plastic yield strength of the till determines the resistance to the moving ice at the subglacial interface and hence plays a key role in determining ice-sheet stability (Tulaczyk et al., 2000b; Bougamont et al., 2011). However, the complex interplay of different physical processes, from granular deformation to pore-water pressure variation and meltwater influx from the frictional heating of the ice, makes the dynamics of the subglacial interface challenging to understand.

The simplest context in which we can study this interplay of processes is a temperate subglacial environment with soft, granular till undergoing shear. We analyze its shear deformation at spatial scales smaller than those of spatially heterogeneous hydrological systems commonly present in subglacial environments (Flowers, 2015). In this limit, the basal resistance to ice motion is governed by the granular mechanics within till. Many laboratory studies target this setting and scale (e.g., N. R. Iverson et al., 1998; Tulaczyk et al., 2000a; Rathbun et al., 2008; N. R. Iverson & Zoet, 2015; Zoet & Iverson, 2020). Theoretical and numerical analyses of granular dynamics are a valuable complement to laboratory studies of subglacial till (MiDi, 2004; da Cruz et al., 2005; Jop et al., 2006; Henann & Kamrin, 2013; Damsgaard et al., 2013, 2015, 2020; Kim & Kamrin, 2020). Critically, most of the existing theoretical analyses focus on much higher strain rates than would be representative of a subglacial environment. Moreover, the theoretical analyses do not consider spatial shear variability within the granular beds, which is ubiquitous in subglacial environments (Engelhardt & Kamb, 1997; Schoof, 2004; Zoet & Iverson, 2020).

One source of spatial shear variability is the changes in stresses and pressures induced by proximal active hydrological drainage systems (Engelhardt & Kamb, 1997; Fischer & Clarke, 2001; Boulton et al., 2001; Mair et al., 2003; Damsgaard et al., 2016). Debris in the basal ice introduces roughness, and correspondingly, also alters shear stresses (N. R. Iverson et al., 2003). Another potential source is shear margins, namely the lateral edges of fast-moving ice streams, where shear strain rates vary notably (Schoof, 2004; Suckale et al., 2014; Perol et al., 2015). Finally, small-scale clasts attached to the base of the ice plough along the subglacial interface and introduce geometrical heterogeneities at the ice-bed interface that contribute to the spatial variability of shear (N. R. Iverson & Hooyer, 2004; N. R. Iverson et al., 2007).

The goal of this study is to advance our process-based understanding of how the porosity of a subglacial granular bed is affected by laterally varying shear speeds. To model the response of a granular bed to laterally varying shear, and, in particular, to capture its macro-scale Coulomb-plastic rheology (Burman et al., 1980; N. R. Iverson et al., 1998; Damsgaard et al., 2013), we use the 3-dimensional Discrete Element Model (DEM) called *Sphere* (Damsgaard et al., 2013). *Sphere* represents the granular bed as a collection of spherical grains that exert elastic and frictional contact forces on each other. We impose a laterally varying velocity profile on the top layer of the grains to introduce spatial shear variability at the bed, and we then estimate the changes in porosity within the sheared granular bed. We neglect thermal processes, focusing only on the granular mechanics as a first step towards a more comprehensive understanding of subglacial till mechanics.

DEMs are standard tools to study the grain-scale dynamics of granular beds (Aharonov & Sparks, 2002; MiDi, 2004; da Cruz et al., 2005; Damsgaard et al., 2013). In conjunction with laboratory experiments, DEMs have led to the identification of the $\mu(I)$ rheology, a phenomenological constitutive model that relates two dimensionless variables, the ratio of shear stress to normal stress, μ, and the inertia number, I, which represents the non-dimensionalized shear strain rate (MiDi, 2004; da Cruz et al., 2005; Jop et al., 2006). Under the local-rheology assumption, which posits that the rheology of the granular medium depends only on the stress and strain rate at a given location (MiDi, 2004), the $\mu(I)$ model provides an appealing, general framework for describing granular homogeneous shear flows across different geometries.

However, the local-rheology assumption becomes problematic in heterogeneous shear flows that arise in the subglacial context. Many subglacial beds exhibit pronounced shear localization (Engelhardt & Kamb, 1998; Boulton et al., 2001) at various depths (Truffer et al., 2000; Truffer & Harrison, 2006). In these shear zones, grains interact non-locally at a small spatial scale, sometimes referred to as a coherence length (e.g., MiDi, 2004). This coherence length is itself spatially variable and dynamic (Orpe & Khakhar, 2001; Ertaş & Halsey, 2002; MiDi, 2004). Local-rheology models like $\mu(I)$ have not been very successful at capturing the properties of shear zones, where non-local behavior becomes important (Jop, 2008), motivating the development of more general, non-local models, such as the one proposed by Henann and Kamrin (2013).

Damsgaard et al. (2020) combined the model of Henann and Kamrin (2013) with a pore-fluid model, providing a framework for describing the interplay between granular mechanics and water percolation in subglacial beds. However, such an approach does not currently entail an evolution equation for porosity. At first sight, that might not appear to be a significant omission, given that prior studies (Silbert et al., 2001; MiDi, 2004; da Cruz et al., 2005; Amarsid et al., 2017; Koval et al., 2009; Azéma & Radjaï, 2014) found that the mean porosity of granular beds is constant for the small inertia numbers characteristic of the subglacial environment (Damsgaard et al., 2013, 2015). A small inertia number indicates a pseudo-static shear regime, where grain contacts persist over relatively long time periods and collisional energy is low. While it is not surprising that the the mean porosity of the bed is less dynamic in this regime, we posit that spatial variability in porosity could still be significant.

Even a slight dependence of porosity on inertia number could have important implications for the subglacial environment. As noted by Damsgaard et al. (2013), since the strength of granular bed depends on the porosity or packing fraction of grains, the more porous parts of a till layer would be more prone to mechanical failure. Failure is relevant not only for understanding sediment flux beneath glaciers and ice streams (Damsgaard et al., 2020), but could also be relevant for understanding the initiation of drainage elements in the granular bed, commonly referred to as canals (Walder & Fowler, 1994; Damsgaard et al., 2017). An important motivation for our work is to better constrain the relationship between porosity and inertia number for the pseudo-static shear regime representative of subglacial environments, especially at the smaller spatial scales which highlight the heterogeneity of such environments.

We emphasize that our study does not represent one particular field site or field setting. Instead, we aim to improve our fundamental understanding of the physical processes contributing to the dynamics of subglacial environments. Subglacial environments are very diverse, ranging from fine-grained remolded marine sediments, for example in West Antarctica (e.g., Tulaczyk et al., 1998; Clarke, 2005), to coarse-grained beds underneath mountain glaciers (e.g., Benn & Owen, 2002). Furthermore, mechanical characteristics are only one part of the dynamics of subglacial environments: thermal characteristics, not considered within this study, substantially affect the ice-bed coupling as well (e.g., Cuffey & Paterson, 2012). Despite the complexities of subglacial environments, DEMs offer a relatively simple means to study the shear dynamics of granular beds at different scales, and may allow us to shed light on some of the processes associated with soft sediments in subglacial environments.

2 Methods

We model the till layer response to spatial shear variation at the ice-till interface using *Sphere*, a DEM developed by Damsgaard et al. (2013), which simulates the deformation of a fluid-saturated granular bed at the grain scale. The granular bed is represented as a collection of $n = 10,000$ spherical Lagrangian particles ("grains") located within a cubical domain of dimensions $L \times L \times L$, where $L = 0.85\,\mathrm{m}$. The grain radii are distributed normally with a mean of $0.02\,\mathrm{m}$ and standard deviation of $10^{-4}\,\mathrm{m}$. The slight variation of grain radius prevents a regular hexagonal packing of grains.

For each grain i, its linear and angular accelerations are resolved by solving Newton's second law,

$$m^i \ddot{\mathbf{x}}^i = m^i \mathbf{g} + \sum_{j=1}^{N} \left(\mathbf{f}_\mathrm{n}^{ij} + \mathbf{f}_\mathrm{t}^{ij} \right) + \mathbf{f}_\mathrm{f}^i \tag{1}$$

$$I^i \dot{\boldsymbol{\omega}}^i = -\sum_j^n (r^i - 0.5\delta_\mathrm{n}^{ij}) \mathbf{n}^{ij} \times \mathbf{f}_\mathrm{t}^{ij}, \tag{2}$$

where m^i [kg] is the grain mass, r^i [m] is the radius, I^i [kg m^2] is the moment of inertia, $\mathbf{x}^i$ [m] is the position vector, $\boldsymbol{\omega}^i$ [1/s] is the angular velocity, and $\mathbf{g}$ [m/s^2] is the gravitational acceleration vector. The vectors $\mathbf{f}_\mathrm{n}^{ij}$ [kg m/s^2] and $\mathbf{f}_\mathrm{t}^{ij}$ [kg m/s^2] are respectively the normal and tangential contact forces between grain i and its neighbor j. The contact forces are modeled as linear elastic forces with a friction-based upper bound on the tangential force (Burman et al., 1980; Damsgaard et al., 2013). We note that, in this model, we do not need to apply viscous damping in parallel to the elasticity and friction, as is done in some DEMs for numerical stability (e.g., Burman et al., 1980; Kruggel-Emden et al., 2007, 2008; Luding, 2008). The vector $\mathbf{n}^{ij} = (\mathbf{x}^i - \mathbf{x}^j)/|\mathbf{x}^i - \mathbf{x}^j|$ is the unit normal contact direction, and δ_n^{ij} [m] is the overlap distance of the grains i and j (Burman et al., 1980; Damsgaard et al., 2013). The vector $\mathbf{f}_\mathrm{f}^i$ [kg m/s^2] is the fluid-grain interaction force,

$$\mathbf{f}_\mathrm{f}^i = -V^i \nabla p(\mathbf{x}^i) - V^i \rho_\mathrm{f} \mathbf{g}, \tag{3}$$

where V^i [m^3] is the volume of grain i, p [Pa] is the fluid pressure deviation from the hydrostatic pressure, referred to as fluid pore pressure for the purposes of this study, and ρ_f [kg/m^3] is the fluid density (Damsgaard et al., 2015). Some studies scale the first term on the right hand side of Eqn. 3 by the local solid fraction to account for the presence of neighboring grains (e.g., McNamara et al., 2000). The solid fraction, however, is of unit order of magnitude, and therefore is omitted in Eqn. 3.

We assess, in Section 3.1, that shear-induced changes in the internal grain skeleton structure do not alter the critical state pore pressure substantially, and therefore the deviations from hydrostatic pore pressure distribution are negligible. As a result, the fluid-grain interaction force in Eqn. 3 reduces to the hydrostatic forcing,

$$\mathbf{f}_\mathrm{f}^i = -V^i \rho_\mathrm{f} \mathbf{g}. \tag{4}$$

2.1 Boundary conditions

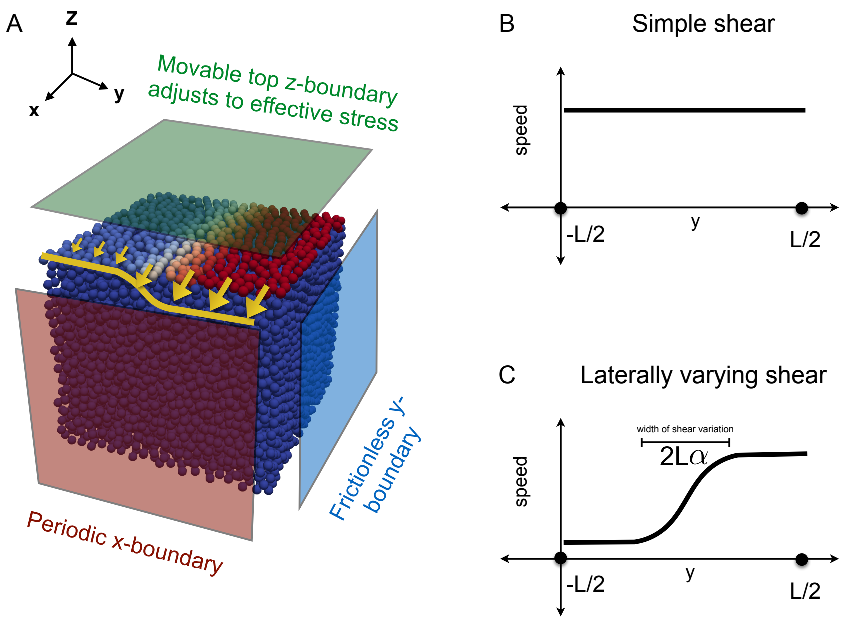

Figure 1. Boundary conditions. (A) Boundary conditions for the grains. The yellow arrows represent the speed profile imposed at the top layer of grains. (B,C) The two speed profiles imposed at the top layer of grains, "simple shear," and "laterally varying shear."

We summarize the boundary conditions in Fig. 1, which are chosen to represent the forcing on a unit of till immediately underneath the glacier sole. The boundaries along the x-axis, the dominant flow direction, are periodic. The lateral ($\pm y$) boundaries and the bottom ($-z$) boundary are fixed in position and are frictionless. The top boundary consists of a wall whose vertical position adjusts dynamically to maintain a prescribed normal stress σ [Pa] on the grain skeleton. Thus, σ represents the effective normal stress imposed on the granular bed.

The granular bed is sheared by the overlying surface (i.e., the "ice/bed interface") moving in the horizontal $+x$ direction. While the nature of shearing in subglacial settings varies substantially both spatially and temporally (N. R. Iverson & Hooyer, 2004; Zoet & Iverson, 2020), we consider an idealized representation. We assign time-invariant velocities in the x-direction for each grain in the top layer. At each time step, we identify all the grains that intersect the top wall and denote them as the 'top layer' grains. For the given time step, these top layer grains are assigned fixed velocities in the horizontal direction but are free to move in vertical direction according to imposed contact forces. Therefore, so long as a grain intersects the top wall, it has a fixed x-speed and zero y-speed. We consider two shear speed profiles for the x-speed of the top layer of grains. The first profile, simple shear (Fig. 1B), imposes on the top layer of grains a constant x-speed v_b. The second profile, laterally varying shear, imposes an increasing speed in the lateral direction (Fig. 1C), from $0.1v_\mathrm{b}$ at $y \le -\alpha L$ to v_b at $y \ge \alpha L$, where α characterizes the relative width of shear variation. Unless otherwise specified, we choose $\alpha = 0.25$ for the laterally varying shear configuration.

2.2 Simplifying till mechanics for numerical modeling

To ensure that the DEM captures the general dynamics of natural granular systems undergoing shear deformation, we perform a non-dimensional analysis where we assess the relative time scales related to the deformation of a saturated granular bed. The inertia number, I (MiDi, 2004; da Cruz et al., 2005; Damsgaard et al., 2013; Azéma & Radjaï, 2014; Damsgaard et al., 2015), represents the shear strain rate normalized by overburden stress and grain density,

$$I = \frac{|\dot{\gamma}|d}{\sqrt{\sigma/\rho_\mathrm{g}}}, \tag{5}$$

where $\dot{\gamma} = v_\mathrm{b}/L$ is the bulk shear strain rate, commonly defined in terms of the shear speed v_b imposed at the top layer of grains. Equivalently, the inertia number also represents the ratio of inertial forces between sediment grains to externally imposed normal forces. Therefore, it characterizes the different regimes in granular deformation. A large inertia number indicates that grain motion is dominated by grain collisions, while a small inertia number characterizes a pseudo-static shear regime, where grain contacts are long-lived and collisional energy is low (Burman et al., 1980). A previous study found the transition between inertial and pseudo-static shear regimes as $I_\mathrm{c} = 2.5{\cdot}10^{-3}$ (Lopera Perez et al., 2016).

We estimate the inertia number for an idealized sandy till undergoing shear deformation. Sandy tills are most akin to DEM models as they have relatively large grain sizes and limited cohesion. Based on the properties of the idealized till, shown in Table 1, we estimate the inertia number as,

$$I_\mathrm{till} < 10^{-6}\,, \tag{6}$$

which is well within the bounds of the pseudo-static shear regime, consistent with prior estimates of deforming subglacial till (Damsgaard et al., 2013, 2015).

We posit that, as long as the inertia number in the DEM simulations is smaller than $I_\mathrm{c} = 2.5 \cdot 10^{-3}$, the granular regime in the simulations is similar to the pseudo-static shear regime of natural till. However, DEMs with low inertia numbers can be computationally time-consuming. To increase the speed of DEM simulations, we perform three modifications. First, we use an approximately unimodal grain size distribution for the

Table 1. Table of parameters, obtained from Damsgaard et al. (2015). The till values correspond to an idealized example of a till. The DEM values correspond to the parameters used for the simulations in this study. Values shown with $\star$ are only used in simulations where granular deformation is coupled with Darcy fluid flow (see Appendix A).

Symbol	Description	Till Value	DEM Value
L	Length of domain. Thickness of actively deforming till layer.	$[0.1, 0.9]\,\mathrm{m}$	$0.85\,\mathrm{m}$
d	Grain diameter.	$[10^{-5}, 10^{-3}]\,\mathrm{m}$	$0.04\,\mathrm{m}$
ρ_f	Density of water.	$1000\,\mathrm{kgm}^{-3}$	$1000\,\mathrm{kgm}^{-3}$
ρ_g	Grain density.	$2600\,\mathrm{kgm}^{-3}$	$2600\,\mathrm{kgm}^{-3}$
ϕ_0	Characteristic porosity.	0.4	0.4 (estimated from simulations.)
v_b	Shear speed.	$[10^{-8}, 10^{-4}]\,\mathrm{m/s}$	$0.085\,\mathrm{m/s}$
$\lvert\dot\gamma\rvert$	Bulk shear strain rate. $\lvert\dot\gamma\rvert = \frac{v_\mathrm{b}}{L}$.	$[10^{-8}, 10^{-3}]\,\mathrm{s}^{-1}$	$0.1\,\mathrm{s}^{-1}$
σ	Effective normal stress imposed by the ice on the till.	[10, 100] kPa	$\{10, 20, 30, 40, 50, 60, 70, 80\}\,\mathrm{kPa}$
I	Inertia number. $I = \frac{\lvert\dot\gamma\rvert d}{\sqrt{\sigma/\rho_\mathrm{g}}}$	$[10^{-17}, 10^{-6}]$	$[10^{-10}, 10^{-2}]$ (estimated from parameter ranges)
β	Bulk compressibility of till.	$[10^{-10}, 10^{-8}]\,\mathrm{Pa}^{-1}$	$^\star 10^{-10}\,\mathrm{Pa}^{-1}$
β_f	Adiabatic fluid compressibility for water at 0°C.	$4.5 \cdot 10^{-10}\,\mathrm{Pa}^{-1}$	$^\star 4.5 \cdot 10^{-10}\,\mathrm{Pa}^{-1}$
η	Dynamic viscosity of water.	$1.787 \cdot 10^{-3}\,\mathrm{Pa \cdot s}$	$^\star 1.787 \cdot 10^{-3}\,\mathrm{Pa \cdot s}$
k_0	Characteristic Permeability.	$\left[10^{-15}, 10^{-13}\right]\,\mathrm{m}^2$	$^\star 10^{-13}\mathrm{m}^2$
τ	Standard deviation of grain radius.	$\left[10^{-4}, 10^{-3}\right]\,\mathrm{m}$	$0.0004\,\mathrm{m}$
κ_n	Grain normal spring stiffness.	$1.16 \cdot 10^9\,\mathrm{Pa \cdot m}$	$1.16 \cdot 10^9\,\mathrm{Pa \cdot m}$
κ_t	Grain tangential spring stiffness.	$1.16 \cdot 10^9\,\mathrm{Pa \cdot m}$	$1.16 \cdot 10^9\,\mathrm{Pa \cdot m}$
λ	Coefficient of grain-grain contact friction.	0.6	0.6

DEM. Real tills have notably wider grain-size distributions (Hooke & Iverson, 1995; Tulaczyk et al., 1998). However, wide grain-size distributions substantially decrease the numerical time step length and increase the cost of grain-grain contacts searches for DEMs (Damsgaard et al., 2013).

Second, we reduce the number of grains in the domain by increasing the mean grain radius over that of sandy till (Table 1). Last, we increase the shear strain rate of the DEM to achieve faster bed deformation relative to subglacial conditions (Table 1). With these modifications, the inertia number of the DEM simulations presented here is estimated as $I_{\mathrm{DEM}} < 0.002$. The inertia number I_{DEM} is larger than that of natural systems, I_{till}, but is less than I_{c}, ensuring that the simulated granular bed is representative of the pseudo-static shear regime associated with till deformation.

2.3 Simulation setup and the computation of quantities

Each DEM simulation consists of three phases. First, we place the grains in the cubic domain and allow them to settle under gravity for 10 s. Next, we consolidate the bed of grains by imposing a uniaxial effective normal stress σ via the top wall for 10 seconds. Finally, we impose the respective shear speed profile on the top layer of grains (Fig. 1B,C) while maintaining a prescribed effective normal stress at the top wall. We run the last phase of the simulations until the porosity becomes quasi-steady, indicating that the granular medium has reached critical state. For visual demonstration, we provide an animation of a DEM simulation where a granular bed undergoes laterally varying shear deformation (see Supplementary Materials).

To understand how shear deformation alters the granular bed, we estimate the porosity, grain velocity, shear strain rate, effective normal stress, and local inertia number of the bed at the end of the simulation. We divide the domain into $1\times10\times10$ rectangular prisms, called cells, and we average each of the above quantities at the cell scale over the last two seconds of the simulation. The relatively small lateral and vertical dimensions of the cell allow us to capture the spatial variability of porosity and the other quantities within the bed. Since the simulations have periodic boundary conditions in the x-direction, each cell spans the entire length of the domain in the x-direction. We do not consider the top layer of grains in our computations since the fixed velocities of those grains may introduce distortions in porosity and the other quantities

To compute the porosity ϕ for a given cell, we add the volumes of each grain centered within the cell, and we add or subtract the partial volumes of the spherical grains intersecting the cell boundaries. We then subtract from, and divide by, the volume of the entire cell (Damsgaard et al., 2013, 2015).

To compute the grain velocity for a given cell at a given simulation time, we record all the grains intersecting the cell at that given time, sum over their displacements over the prior two seconds, then divide by the two seconds and the number of grains. Using net displacement provides a smoother estimate of grain velocity than the instantaneous values resulting from erratic grain collisions. To compute the lateral and vertical shear strain rates for a cell, we use a forward difference scheme on the grain velocities in the lateral and vertical directions, respectively.

We estimate the vertical effective normal stress σ acting on a cell as the sum of the effective normal stress imposed on the top of the bed, and the weight of the sediment within the overlying column of cells. The latter is computed by integrating over the product of the grain density, the volume, and the solid fraction, $1-\phi$, of the overlying column.

We compute the local inertia number for each cell by first computing the cell-specific cumulative shear strain rate and effective normal stress for the respective cell (see Eqn. (5)).

To approximate the cumulative shear strain rate of the cell, we sum the absolute values of the lateral and vertical shear strain rates. The computation of the true shear strain rate involves additional strain rate components. However, given that the shear is applied in x-direction, we argue that the components other than the lateral and vertical shear strain rates in the x-direction are negligible, and that the approximate form provides a similar shear strain rate distribution to the true value.

2.4 Model limitations

We use our DEM to highlight some of the subglacial dynamics associated with porosity that arise from the granular dynamics of soft, temperate, water-saturated till. However, the assumptions and simplifications within our model limit the general validity of our results. Subglacial settings vary widely from region to region, with substantial differences in till composition, stress distribution, and hydrology. Instead of representing one particular subglacial setting, our model represents a generic, highly idealized subglacial till layer whose characteristics are within the range of those for real subglacial settings.

Some subglacial settings have substantial variability in grain sizes (Tulaczyk et al., 1998). However, since DEMs are computationally expensive, we use an effectively unimodal normal grain-size distribution and increase the grain size. The model is hence more suitable to represent behavior associated with sandy tills, such as the Caesar till in Ohio, USA (Rathbun et al., 2008), than tills with a high clay content (Tulaczyk et al., 1998). For example, tills composed entirely of clay platelets may deform very differently than those with spherical grains, given the distinct geometry of platelets. Tills with a mixed composition may also have reduced porosity since the clay platelets fill up the pore spaces between the silt grains (Crawford et al., 2002, 2008), a process which we do not include in our model.

Our model does not capture the variability of large-scale hydrological systems that might exist at the subglacial interface (e.g., Flowers, 2015). While systems of channels or canals (Walder & Fowler, 1994; Ng, 2000) may generate spikes in pore pressure that can trigger rapid deformation of the granular bed (e.g., Engelhardt & Kamb, 1997; Truffer et al., 2000; Tulaczyk et al., 2000a; Damsgaard et al., 2020), they operate at larger scales than the system that we study here. Instead, we assume hydrostatic pore pressure within the till, allowing us to focus on the first-order granular dynamics of subglacial beds.

3 Results

3.1 Pore pressure equilibrates substantially faster than grains rearrange

The pore space of a temperate subglacial till layer is saturated with meltwater. Deformation of the grain skeleton and the corresponding changes in pore space may alter the pore pressure and cause it to deviate from a hydrostatic profile. To estimate the degree to which the pore pressure deviates from the hydrostatic profile during critical-state shear, we explore the temporal evolution of the pore pressure as expressed by Goren et al. (2011) and Damsgaard et al. (2015):

$$\frac{\partial p}{\partial t} = \frac{1}{\beta_{\mathrm{f}} \phi \eta} \nabla \cdot (k \nabla p) - \frac{1}{\beta_{\mathrm{f}} \phi (1-\phi)} \left(\frac{\partial \phi}{\partial t} + \overline{\mathbf{v}} \cdot \nabla \phi \right), \tag{7}$$

where t [s] is time, β_{f} [1/Pa] is the adiabatic fluid compressibility, $\overline{\mathbf{v}}$ [m/s] is the mean grain velocity, and ϕ is the porosity. The first term on the right hand side represents spatial equilibration of pressure within the fluid through Darcian diffusion. The second term represents the forcing by the deforming grain skeleton.

We perform a non-dimensional analysis of Eqn. (7) to compare the time scales of the two processes, spatial pore pressure equilibration, and grain skeleton forcing. The characteristical scales for the variables in Eqn. (7) are chosen based on the idealized till properties from Table 1,

$$p = \frac{\hat{p}}{\beta}, \quad \mathbf{u} = \hat{\mathbf{u}} v_\mathrm{b}, \quad k = \hat{k} k_0, \quad t = \hat{t} t_0, \tag{8}$$

where the hat notation marks non-dimensional variables, β is the bulk compressibility of the granular material, d, the mean grain diameter, is taken as the characteristic length scale, $t_0 = d/v_\mathrm{b}$ is taken as the characteristic time scale, and k_0 as the characteristic permeability. Non-dimensionalization of Eqn. (7) yields,

$$\frac{\partial \hat{p}}{\partial \hat{t}} = \frac{k_0}{\beta_\mathrm{f} \phi \eta d v_\mathrm{b}} \hat{\nabla} \cdot \left(\hat{k} \hat{\nabla} \hat{p} \right) - \frac{\beta}{\beta_\mathrm{f} \phi (1-\phi)} \left(\frac{\partial \phi}{\partial \hat{t}} + \hat{\bar{\mathbf{v}}} \cdot \hat{\nabla} \phi \right). \tag{9}$$

The non-dimensional Deborah number (Goren et al., 2010) arises as the inverse of the coefficient of the first term on the right-hand side,

$$\mathrm{De} = \frac{\beta_\mathrm{f} \phi \eta d v_\mathrm{b}}{k_0}. \tag{10}$$

The Deborah number represents the ratio of the time scale of pore pressure diffusion to the time scale associated with pore pressure changes resulting from changes in pore volume. In our case, changes in pore volume arise in response to the shear imposed on the top boundary. To specifically account for the compressibility of the deforming grain skeleton, which is expected to limit pore fluid pressurization, we define a modified Deborah number, De^s, by taking the ratio of the coefficients of the first and second terms on the right hand side of Eqn. 9,

$$\mathrm{De}^\mathrm{s} = \frac{\beta \eta d v_\mathrm{b}}{k_0 (1-\phi)}. \tag{11}$$

We estimate the modified Deborah number, $\mathrm{De}^\mathrm{s}_\mathrm{till}$, based on the values gives in Table 1,

$$\mathrm{De}^\mathrm{s}_\mathrm{till} < 0.003. \tag{12}$$

The small value of the modified Deborah number indicates that the pore fluid pressure of the till diffuses and equilibrates almost instantaneously with respect to changes in the grain skeleton structure at the grain scale. As a result, changes to the grain skeleton structure of the till have a negligible impact on the pore pressure. Consequently, in the absence of external pressure gradients, the pore fluid acts only as a source of buoyancy force on the grains, as characterized by Eqn. (4).

The above analysis applies to the example of the idealized sandy till described in Table 1. To show that our finding of a low Deborah number and rapid pore pressure equilibration applies to a relatively wide variety of subglacial settings, we perform a similar computation of the Deborah number for clay-rich till. Here, we consider the till underneath Whillans Ice Stream as an example. The bulk compressibility of the till is within the range $10^{-9}\,\mathrm{Pa}^{-1} < \beta < 10^{-7}\,\mathrm{Pa}^{-1}$ (Leeman et al., 2016), and the dynamic viscosity of water at 0° is $1.787 \cdot 10^{-3}$ Pa s (Table 1). Since the till underneath Whillans Ice Stream consists predominantly of silt and clay, the characteristic grain diameter lies within the range $10^{-6}\mathrm{m} < d < 10^{-5}\mathrm{m}$ (Tulaczyk et al., 1998). We consider an ice-stream like range of velocities for the top layer of grains of the till $10^{-8}\,\mathrm{m/s} < v_b < 10^{-4}\,\mathrm{m/s}$ (Scheuchl et al., 2012). The characteristic permeability of the till lies within the range $10^{-17}\,\mathrm{m}^2 < k_0 < 10^{-13}\,\mathrm{m}^2$ (Leeman et al., 2016). Using Eqn. 11, we get,

$$\mathrm{De}^\mathrm{s}_\mathrm{WIS} < 0.03 \tag{13}$$

This analysis suggests that a wide range of subglacial tills exhibit low Deborah numbers, and likely experience near-instantaneous pressure equilibration during critical-state shear.

In the absence of external pressure gradients, the fluid pressure distribution within the granular bed would thus remain hydrostatic during critical state shear.

Based on the above analysis, our DEM solver decouples the granular motion from the fluid flow and imposes a hydrostatic profile for the latter (Eq. 4). To verify the assumed link between a low Deborah number and hydrostatic pressure conditions, we run a simulation with a fully coupled DEM solver. As is done in (Damsgaard et al., 2015), the coupled solver uses Eqns. 3 and 7 to compute the fluid pressure distribution at each step. The details for the coupled solver and the associated boundary conditions are provided in Appendix A. The fluid pressure-distribution at the end of the fully coupled simulation, shown in Fig. A1, resembles hydrostatic pressure conditions, supporting the assessment that low Deborah number systems have approximately hydrostatic pressure at critical state.

3.2 At low normal stresses, shear zone thickness increases with normal stress

We conduct simple shear simulations to establish a reference point for understanding how laterally varying shear alters the local porosity and strain rate values within a deforming granular bed. Fig. 2 summarizes the kinematic and geometric measurements of velocity, strain rate, and porosity, averaged over the last two seconds of the simulations ($18\,\mathrm{s} < t < 20\,\mathrm{s}$) for effective normal stresses of $\sigma = 10, 50\,\mathrm{kPa}$ and shear velocity $v_b = 0.085$ m/s for the top layer of grains (see Table 1). Panels A and B show that grain speed along the x-direction decreases with depth near the top boundary. The difference between the two panels highlights that, as the effective normal stress increases, grains deeper within the bed are mobilized during shear.

Figs. 2C and D show the shear strain rates for the same simulations. For $\sigma = 50\,\mathrm{kPa}$, the shear strain rate is approximately constant over a depth of 0.15m (Fig. 2D). The shear strain rate near the top boundary is greater for the $\sigma = 10\,\mathrm{kPa}$ simulation, consistent with the shallower depth of deformation penetration.

Figs. 2E and F show the porosities of the granular bed. The porosities are elevated near the top boundary in both panels, but the zone of elevated porosity is thicker in the higher effective normal stress simulation. The largest porosities are found in the areas with the largest shear strain rates. Taken together, the simple shear simulation results suggest that the shear zone and the corresponding zone of elevated porosity increase in thickness with increasing effective normal stress, at least for the relatively small effective normal stresses applied here.

We plot shear zone thickness against effective normal stress for 8 simple shear simulations with effective normal stresses $\sigma = 10, 20, ..., 80$ kPa in Fig. 3. The figure estimates shear zone thickness as the depth to which the shear strain rate is greater than 10% of the maximum shear strain rate value for the given simple shear simulation. Since the shear strain rates are computed at the cell-scale in Fig. 2, we average across width and interpolate the shear strain rates across the cells with an exponential fit. The figure shows that shear zone thickness increases with effective normal stress for $\sigma < 60\,\mathrm{kPa}$. For higher values of normal stresses, shear zone thickness appears to decrease slightly. We present the entire range of simulation results, including grain velocity, shear strain rates, and porosity, in Fig. B1.

Fig. 4 shows the mean porosity of the upper half of the granular bed against time. It indicates that simulations start with an initial dilation stage lasting for up to $t = 5\,\mathrm{s}$ for all effective normal stresses, after which the mean porosity remains approximately constant. The mean porosity is lowest for the case of $\sigma = 10\,\mathrm{kPa}$, with a value of 0.405 around $t = 20\,\mathrm{s}$. Although the porosity values around $t = 20\,\mathrm{s}$ vary considerably with effective normal stress, the range of variability is less than 0.007. Overall, there is no clearly

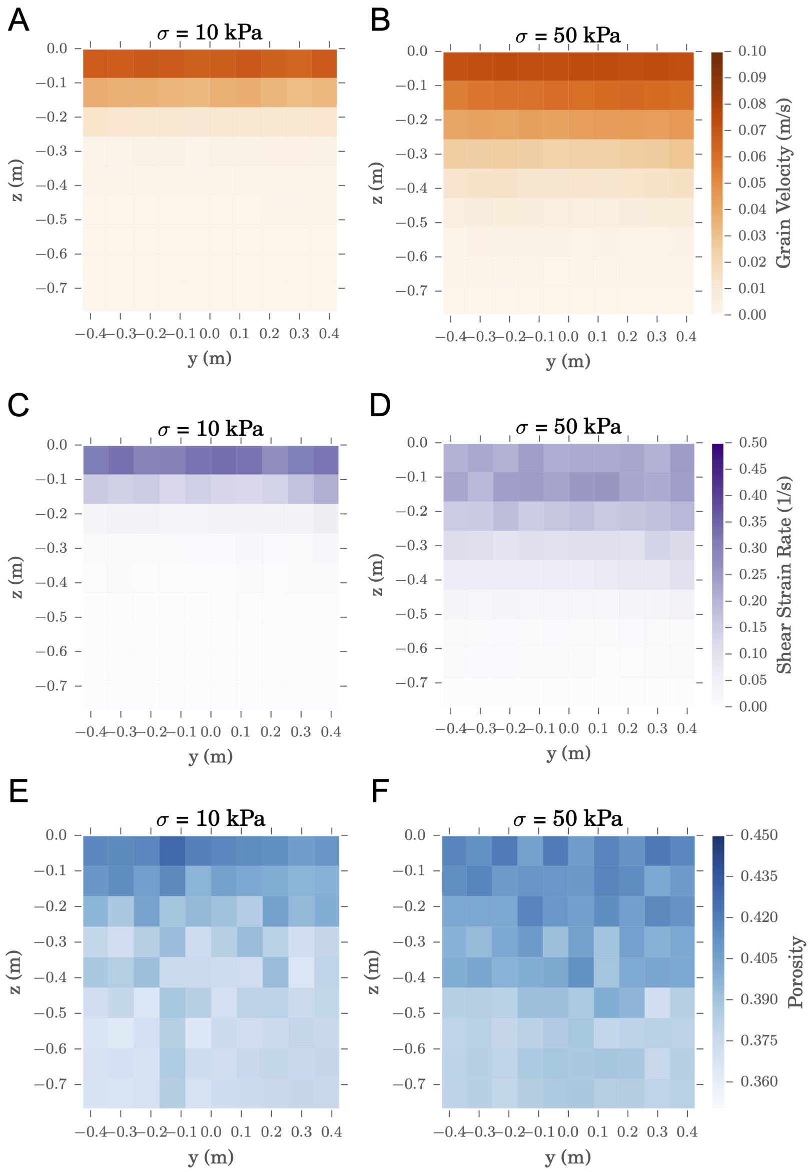

Figure 2. Simulation results for the simple shear configuration (Fig. 1B). (A,B) Grain speeds in the x-direction, averaged along the x–axis, for effective normal stresses of 10 kPa and 50 kPa respectively. (C,D) Shear strain rates for the respective effective normal stresses, approximated as the sum of absolute values of y– and z–gradients of velocities in the x-direction. (E,F) Porosities for the respective effective normal stresses. All variables are averaged over the simulation time $18\,\text{s} < t < 20\,\text{s}$. The top layer of grains, for which a time-invariant speed profile is imposed as a boundary condition, are not shown in the panels.

discernable relationship between porosity and effective normal stress over the relatively small range of effective normal stresses considered in this study.

To ensure that our results are not impacted by boundary effects arising from limited bed thickness, we conduct additional DEM simulations with thicker beds. Our re-

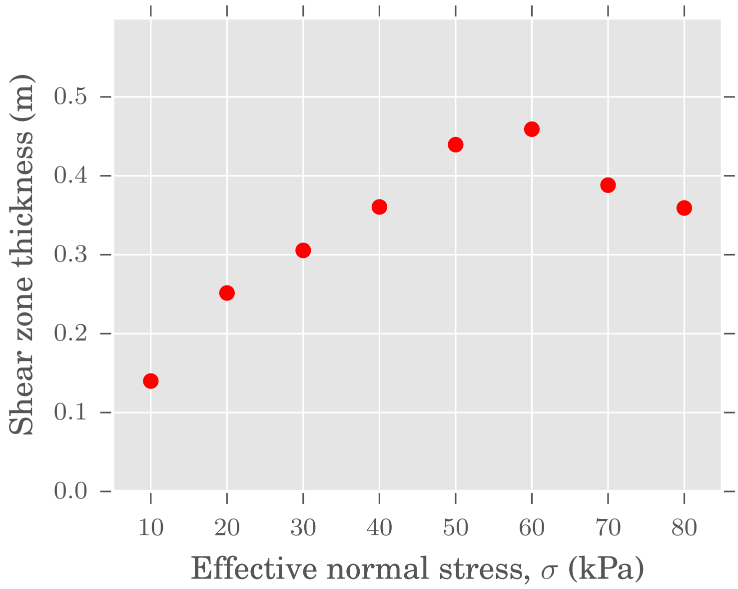

Figure 3. Shear zone thickness for different effective normal stresses in the simple shear configuration. The shear zone thickness of a bed undergoing simple shear is computed as the depth at which the width-averaged shear strain rate drops to 10% of the maximum strain rate value.

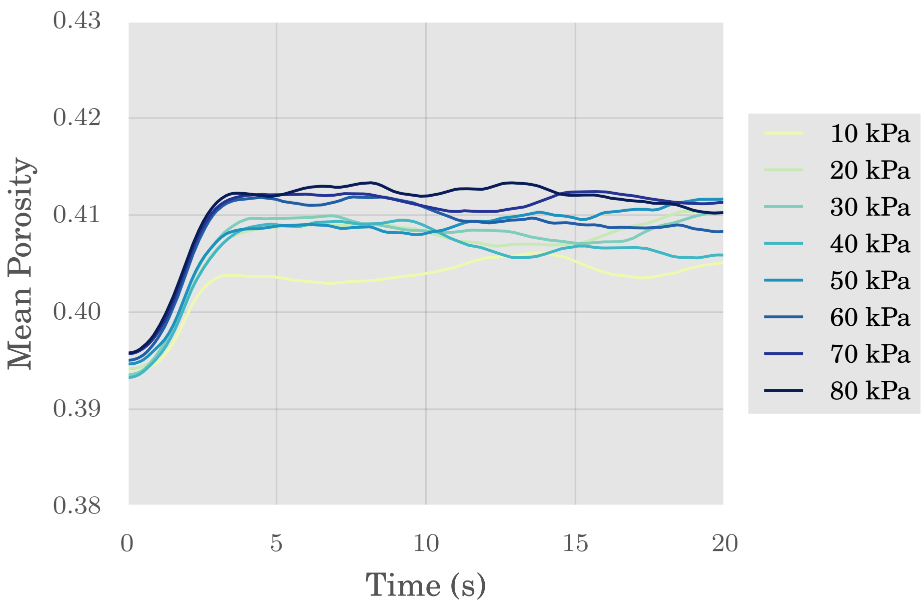

Figure 4. Temporal evolution of porosity for the simple shear configuration, shown in terms of the mean porosity for the upper half of the granular bed. The temporal values are smoothed with a moving average window of $t = 4\,\mathrm{s}$.

sults in Appendix C show that grain velocities remain unchanged with thicker beds, suggesting that there are no associated vertical boundary effects within the domain. Similarly, DEM simulations with wider beds in Appendix D show that having fixed, frictionless lateral boundaries does not affect the distribution of shear strain rate and porosity within the bed.

3.3 Lateral shear variation at the ice-till interface creates narrow zones of elevated porosity

To understand how lateral shear variation affects the porosity within a granular bed, we describe the results of simulations with a laterally varying shear profile, as shown in Fig. 1C. Grain speeds increase across the lateral direction and decrease along the depth, as seen in Fig. 5A,B. The computed shear strain rates vary laterally, decrease with depth, and attain maximum values close around the lateral center of the top boundary ($y = 0, z = 0$), as seen in Fig. 5C,D. The highest porosity values are located near the cells with the largest shear strain rates (Fig. 5E,F).

We present the vertical and lateral shear strain rates in Fig. 6. The vertical shear strain rates, shown in panels A and B, increase from the left to the center of the domain and then decrease slightly at the right side of the domain. The largest vertical strain rates are located near the top boundary ($z = 0$). The lateral shear strain rates, shown in Figs. 6C and D, are highest near the top boundary at the lateral center of the shear variation ($y = 0, z = 0$), and decay to zero away from the center. The magnitudes of the vertical and lateral shear strain rates do not change notably with the effective normal stress. However, the panels suggest that both lateral and vertical shearing occurs deeper within the granular bed at higher effective normal stresses.

Fig. 7 depicts the temporal evolution of the mean porosity for the lateral shear configuration over a simulation time of 50 s. The mean porosity shows a greater variability than in the simple shear configuration (Fig. 4). The porosity continues to increase until $t = 40\,\mathrm{s}$ ($t > 48\,\mathrm{s}$ for the $\sigma = 10\,\mathrm{kPa}$ simulation), after which they attain critical state. As in the case of simple shear, the mean porosity varies by less than 0.007 across the range of effective normal stresses at the end of the simulations.

To understand how the spatial extent of the laterally varying shear affects porosities, we perform another set of simulations where the applied shear varies laterally over a larger width ($\alpha = 0.5$, see Fig. 1C). The simulation results, presented in Fig. 8, show three differences with respect to the results in Fig. 5, namely, the deformation is spread out in the lateral direction; the shear strain rates (Figs. 8C and D) are smaller in magnitude with respect to the more localized variable shear (Figs. 5C and D); and the zone of elevated porosity in Figs. 8E and F is also wider than in Figs. 5E and F.

3.4 Porosity scales with local inertia number in the pseudo-static shear regime

Previous studies have explored the dependence of porosity on inertia number in the context of homogeneous shear flows (MiDi, 2004; da Cruz et al., 2005; Azéma & Radjaï, 2014). These studies find an increasing relationship between mean porosity and inertia number for $I > I_\mathrm{c}$ and suggest that the mean porosity is approximately independent of inertia number for $I < I_\mathrm{c}$. However, these prior studies do not directly apply to heterogeneous shear flows, as considered in our study, where shear localizes and porosity varies spatially.

To estimate the relationship between porosity and inertia number for an idealized subglacial bed, we compute both variables locally. More specifically, we compute porosity (ϕ) and local inertia number (I_local) at the spatial scale of cells, as shown in Fig. B1 (see Section 2.3 for more details). Fig. 9 shows our results in the form of scatter plots

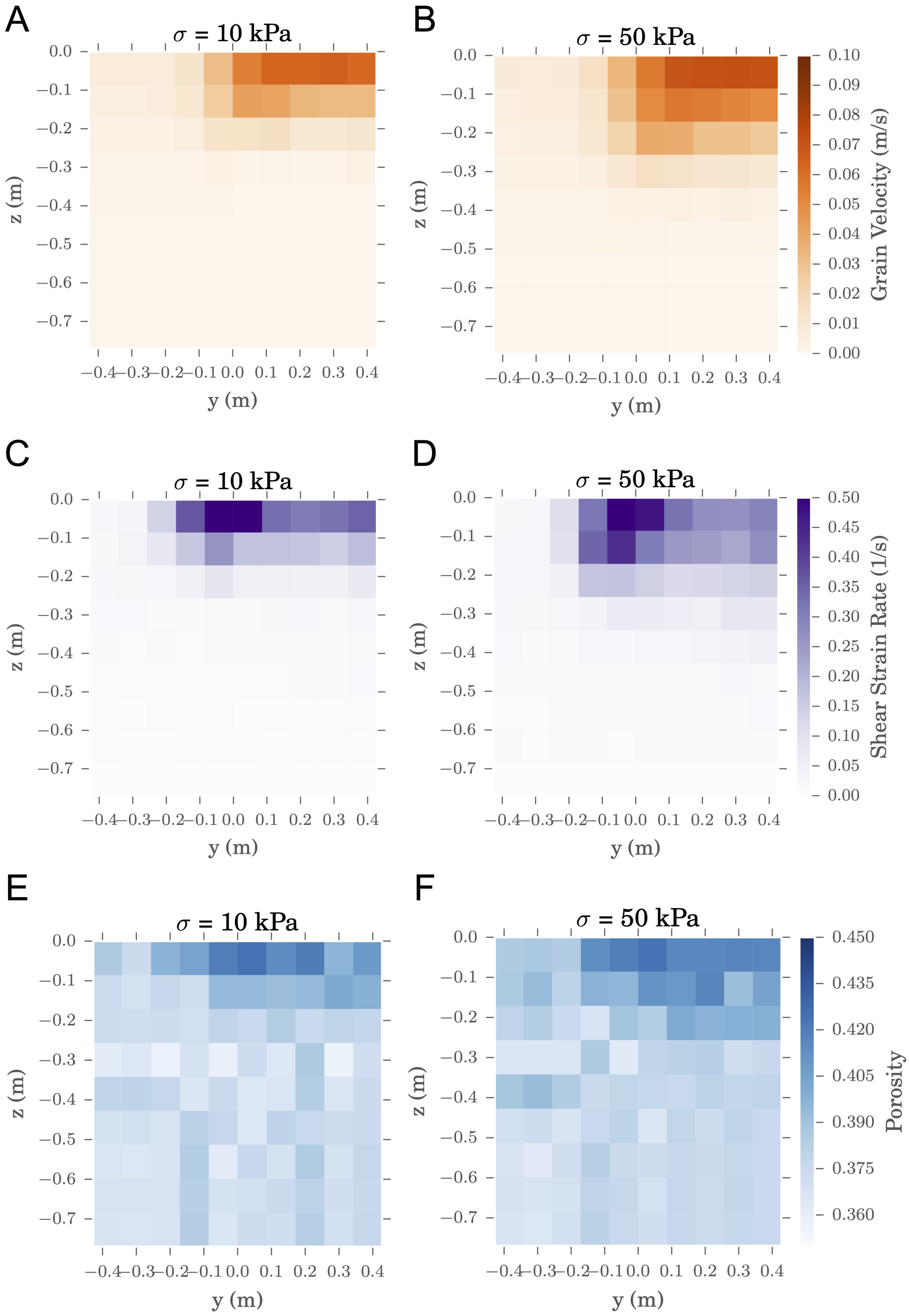

Figure 5. Simulation results for the laterally varying shear configuration (Fig. 1C). (A,B) Speed of the grains in the x-direction, for effective normal stresses of 10 kPa and 50 kPa respectively. (C,D) Shear strain rates for the respective effective normal stresses, approximated as sum of absolute values of y and z-gradients of velocities in the x-direction (See Section 2.3 for more details). (E,F) Porosities for the respective effective normal stresses. The top layer of grains, where the boundary condition is imposed, are not shown in the panels.

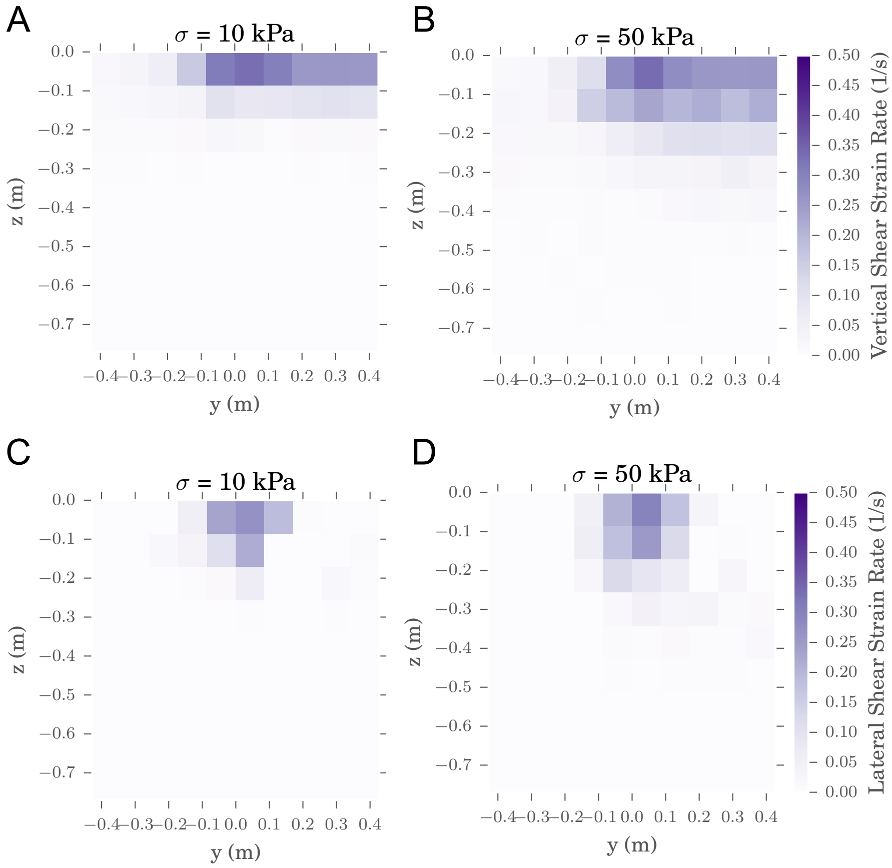

Figure 6. Components of the shear strain rate for the laterally varying shear configuration. (A,B) Vertical shear strain rate, for effective normal stress of 10 kPa and 50 kPa respectively. (C,D) Lateral shear strain rate, for effective normal stress of 10 kPa and 50 kPa respectively.

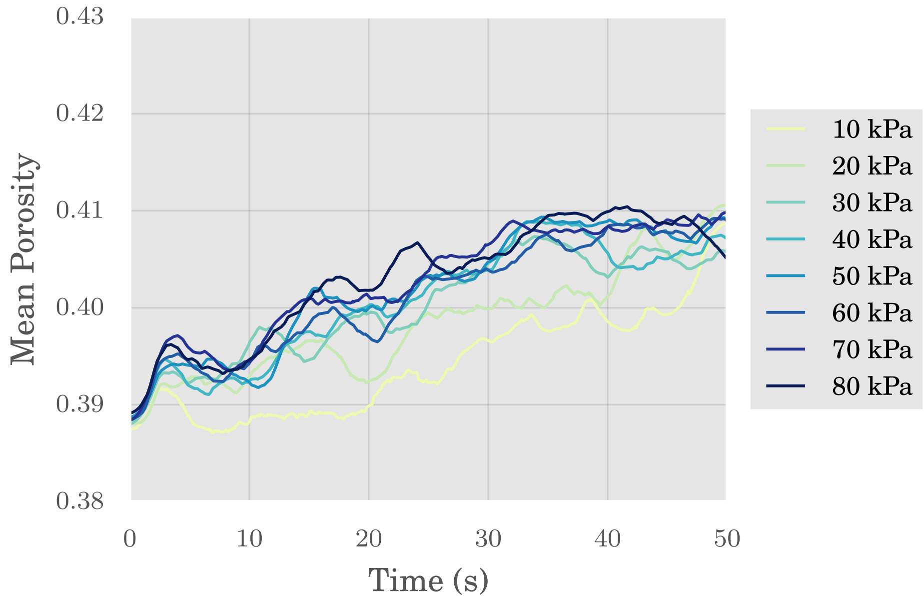

Figure 7. Temporal evolution of porosity for the laterally varying shear configuration, shown in terms of the mean porosity for the upper half of the granular bed. The temporal values are smoothed with a moving average window of $t = 4\,\mathrm{s}$.

of these local variables for different shear distributions and normal stresses. To avoid confounding the analysis with boundary effects, we have removed the data adjacent to the lateral and vertical boundaries of the domain. Despite the substantial variability in porosity, the panels indicate an overall increase in porosity with local inertia number in both the simple shear and laterally varying shear configurations, and for both effective normal stresses ($\sigma = 10\,\mathrm{kPa}$ and $50\,\mathrm{kPa}$).

All the simulations in Fig. 9 exhibit an approximately linear dependence between the porosity and the logarithm of the local inertia number, suggesting a common relationship between the two variables across different effective normal stresses and shear configurations. To further explore this possibility, Fig. 10A shows the relation between these two local variables when combining the results of several simulations. We find an overall common trend, $\phi \approx 0.01 \ln I_{\mathrm{local}} + 0.48$, with a least squares linear regression correlation coefficient of $\mathrm{R}^2 = 0.81$. We note that the trend is only valid within the investigated pseudo-static shear regime of a non-zero but finite local inertia number, namely, $I_{\mathrm{local}} < 2.5 \cdot 10^{-3}$, and does not apply to the regime $I_{\mathrm{local}} \to 0$.

In contrast to the clear correlation between the porosity and local inertia number suggested by Fig. 10A, no such relationship exists between the two variables when averaged over the domain scale. Fig. 10B shows the porosity and inertia number averaged over the upper half of the granular bed for simulations with both simple shear and laterally varying configurations and different values of effective normal stresses. The data show a single cluster with no discernible trends.

The contrast between the local scale (Fig. 10A) and the domain scale (Fig. 10B) stems from the inability of the latter to capture localized dynamics within the granular bed. The spatial distribution of a laterally varying shear and the balance of gravitational forces across the shear zone thickness are two examples of localized dynamics that act at scales smaller than that of the entire domain. We find here that the prop-

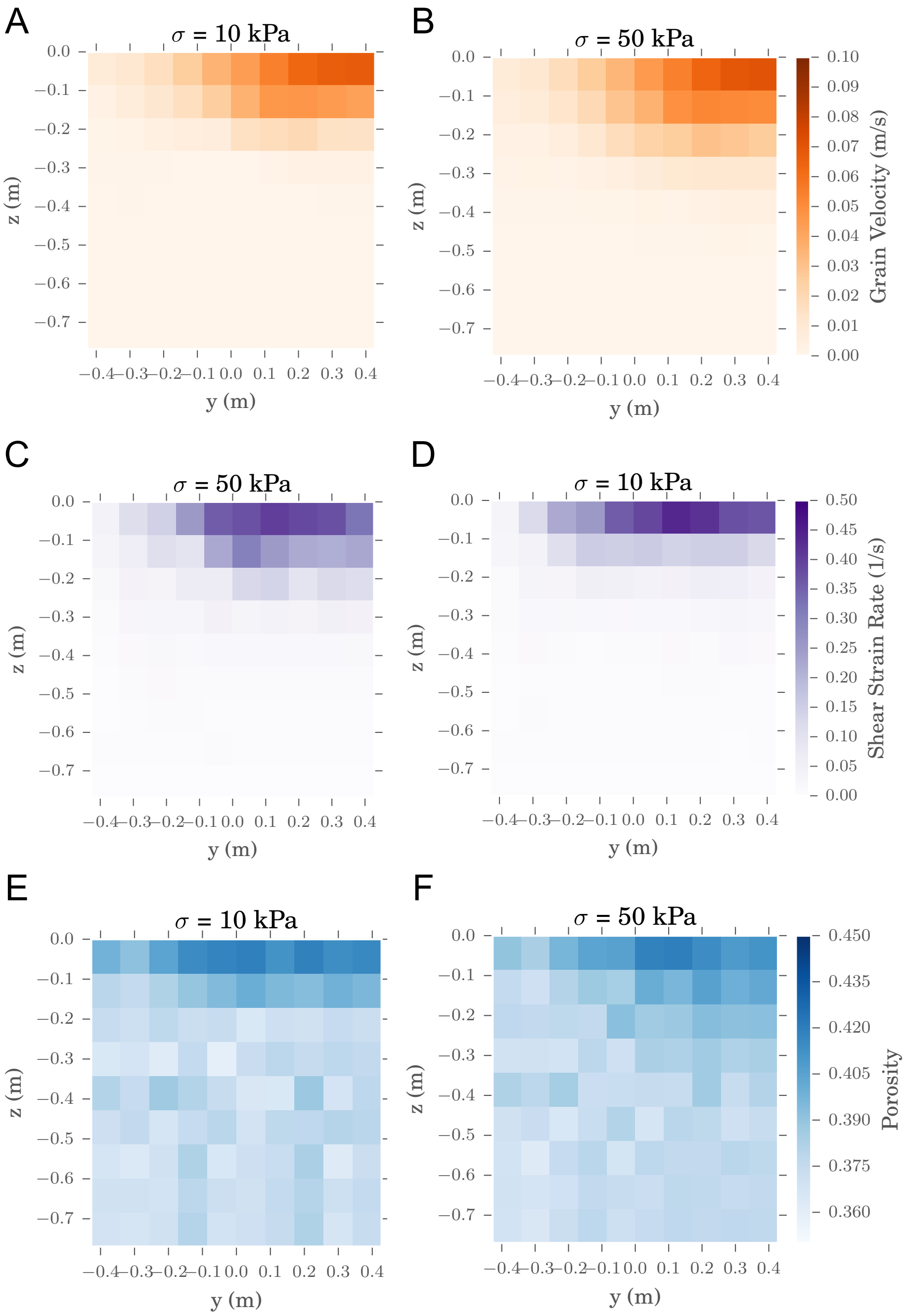

Figure 8. Simulation results for the configuration of wide, laterally varying shear ($\alpha = 0.5$) at the ice-till interface (Fig. 1D). (A,B) Speed of the grains in the x–direction, for effective normal stress of 10 kPa and 50 kPa respectively. (C,D) Shear strain rates for the respective effective normal stresses, approximated as sum of absolute values of y– and z–gradients of velocities in the x–direction (See Section 2.3 for more details). (E,F) Porosities for the respective effective normal stresses.

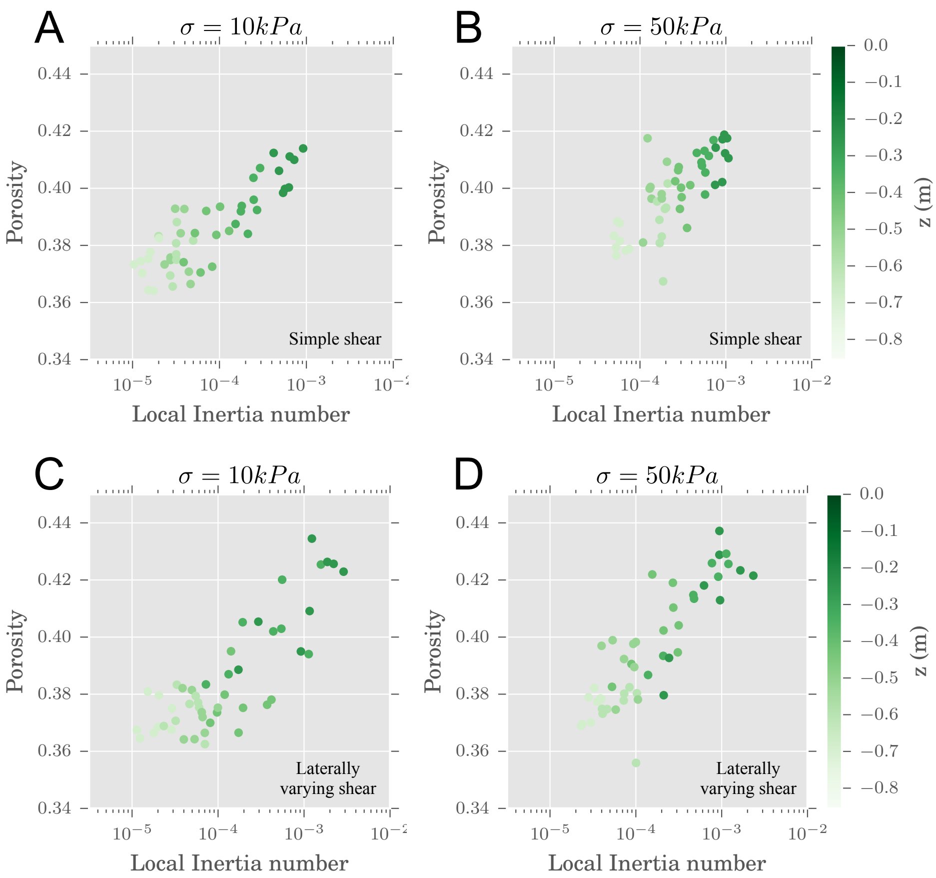

Figure 9. Porosity ϕ vs. local inertia number I_{local} for the cells of the DEM simulations. (A,B) Simple shear for $\sigma = 10\,\text{kPa}$ and $\sigma = 50\,\text{kPa}$, respectively. (C,D) Laterally varying shear for the same effective normal stresses. Values obtained by averaging over the last two seconds of each simulation.

erties of the zone of localized deformation are not well represented through domain-averaged quantities, highlighting the importance of estimating porosity and inertia number at local scales under non-homogeneous conditions.

4 Discussion

The interactions between granular deformation and pore fluid flow can be complex, but most of these complexities arise during the onset of deformation or in the limits of a high inertia number (N. R. Iverson, 2010; Houssais et al., 2015; Baumgarten & Kamrin, 2019). Subglacial beds are characterized by low inertia numbers, suggesting that they are in a pseudo-static regime where porosity is less prone to dynamic readjustments than at high inertia numbers. However, shear at the subglacial interface can vary spatially. We show here that spatial shear variation creates a narrow zone within the bed with increased porosity, even in the pseudo-static regime. We explain this behavior by demonstrating that a common power-law relationship connects porosity and inertia number across different shear configurations and effective normal stresses.

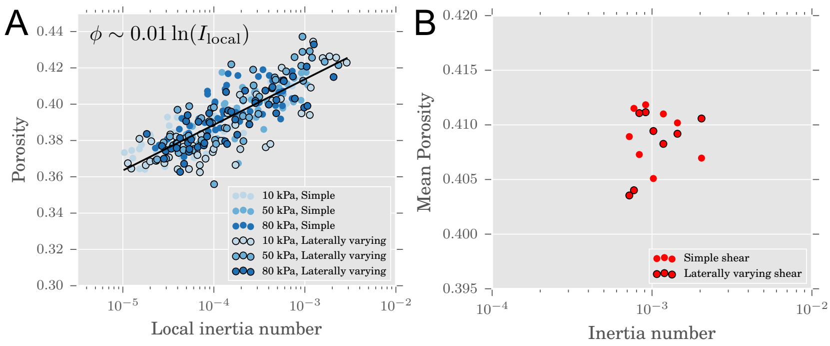

Figure 10. Porosity and inertia number for DEM simulations superimposed together. (A) Scatter plot for porosity and inertia number at the local scale. The simulations include the simple and laterally varying shear configurations for effective normal stresses 10, 50, and 80kPa respectively. The trendline, shown in black, is calculated with ordinary least squares linear regression in semi-log scale. (B) Scatter plot for porosity and inertia number averaged over the upper half of the domain. The simulations include 8 effective normal stresses, 10 to 80kPa.

4.1 Spatially variable shear can facilitate more efficient meltwater drainage

Temperate subglacial environments exhibit complex coupled dynamics of ice motion, meltwater drainage, and till deformation (Clarke, 2005). The yield strength of the till determines the frictional resistance to the motion of the ice, and porosity plays a key role in determining this strength, given the Coulomb-frictional rheology of till (N. R. Iverson et al., 1998; Tulaczyk et al., 2000a). Established models of glacier beds, such as the undrained plastic bed model by Tulaczyk et al. (2000b), assume that till porosity is governed by the effective normal stress through compression (Tulaczyk et al., 2000b; Leeman et al., 2016).

Our results show that other physical processes introduce important variability into the till porosity, particularly in the immediate vicinity of the subglacial interface. Some subglacial environments experience spatially variable shear strain rates, such as shear margins (Jacobson & Raymond, 1998; Schoof, 2004; Suckale et al., 2014; Haseloff et al., 2018) or regions with clasts ploughing along the subglacial interface (N. R. Iverson & Hooyer, 2004; N. R. Iverson et al., 2007). The shear stress imposed by the moving ice on the till alters porosity through shear dilation, even in the pseudo-static regime (Fig. 2). At a granular scale, the reason for the increased porosity is the increase in velocity fluctuations of grains near the shear interface, where the inertia number is relatively high (Jenkins & Savage, 1983; Gaume et al., 2011; Kim & Kamrin, 2020).

Our study captures the spatial variations of the porosity and inertia number within the granular bed at a scale larger than grain size but smaller than the domain size. Spatial averaging over the domain size masks the non-local behavior occurring at scales smaller than the entire bed, and with it, the relationship connecting porosity and inertia number at the local scale. Our local-scale results highlight the $\phi(I_{\mathrm{local}})$ relationship where porosity increases with the inertia number in the pseudo-static shear regime. The finding is consistent across both the simple shear and laterally varying shear configurations, suggesting a common relationship between porosity and local inertia number that is applicable for heterogeneous shear flows within the pseudo-static regime (Fig. 10A).

The increase in the porosity of a granular bed, especially within a narrow zone for the case of a laterally varying shear (Fig. 5), has two potential implications for meltwater flux within subglacial till. First, the increase in till porosity is likely to cause a corresponding increase in till permeability, increasing the flux of meltwater through the pores of the till. For granular beds composed of silt or sand, the Kozeny-Carman relationship suggests that the permeability scales with the cube of porosity (Kozeny, 1927; Carman, 1937; Costa, 2006). However, beds with a high clay content, especially those underneath West Antarctic ice streams (Tulaczyk et al., 1998; Lindeque et al., 2016), may not experience a similar increase in permeability because clay platelets can block pores and mitigate any corresponding increase in porosity (Crawford et al., 2002, 2008).

Second, the increase in porosity in a relatively narrow zone can localize fluid flow by acting as a preferential pathway for meltwater. Due to the increased porosity, shown in Fig. 5, the granular material here is arranged in a weaker packing configuration and is thus more susceptible to plastic failure than in the neighboring regions. Failure may be triggered by potential spikes in pore pressure gradients caused by external hydrological processes. Such pressure spikes are commonly observed in boreholes (Engelhardt & Kamb, 1997). The plastic failure of a narrow zone of increased porosity could initiate canal-like drainage structures incised into the till (Walder & Fowler, 1994; Ng, 2000; Damsgaard et al., 2017), facilitating more efficient drainage of meltwater. Capturing the plastic failure instability and the subsequent potential drainage formation, however, is beyond the capability of this model.

Many prior models exist that integrate distributed and channelized water transport (Hewitt, 2011; Hewitt et al., 2012a, 2012b; Werder et al., 2013). However, it is not clear how subglacial channels or canals (Walder & Fowler, 1994) initiate. While some studies have considered the role of thermal (Walder, 1982; Walder & Fowler, 1994) and erosional instabilities (Kasmalkar et al., 2019) that could lead to the formation of subglacial drainage systems, the role of till deformation and coupled porous fluid flow has been less explored. Our simulations suggest that canals could initiate through plastic failure in the regions experiencing spatially variable shear strain rates, such as shear margins (Jacobson & Raymond, 1998; Schoof, 2004; Suckale et al., 2014; Haseloff et al., 2018), or regions with ploughing clasts or ice keels (N. R. Iverson & Hooyer, 2004; N. R. Iverson et al., 2007).

4.2 Pore pressure equilibrates near-instantaneously within deforming subglacial till

For glaciers with temperate beds and fine-grained sediments constituting the till layer, the pore water pressure within the till plays an important role, because it alters the basal resistance to the overlying ice (e.g., Tulaczyk et al., 1998, 2000a). Deformation of the grain skeleton structure affects the pore spaces, which, in turn, causes small-scale deviations in the pore water pressure that diffuse spatially across the neighboring pores (N. R. Iverson et al., 1998; Moore & Iverson, 2002; Damsgaard et al., 2015).

Granular deformation and pore fluid pressure equilibration tend to operate on different time scales. Previous studies proposed that dilation associated with adjustment to the critical state can cause bed strengthening behavior (N. R. Iverson et al., 1998; Moore & Iverson, 2002; N. R. Iverson, 2010; Damsgaard et al., 2015), where shear dilation of the till expands pore spaces, and causes a reduction of the water pressure within the pores. This mechanism of bed strengthening applies if the changes in the grain skeleton structure occur faster than the spatial equilibration of pore pressure. To quantify the competition between the two processes during critical-state shear, when porosity is quasi-steady, we estimate the Deborah number that expresses the ratio between the time scales of pore pressure diffusion and of skeleton deformation (Goren et al., 2010).

Our computations for the critical state deformation show that the Deborah number is small for a wide range of subglacial settings, from coarse-grained till, $\mathrm{De}^{\mathrm{s}}_{\mathrm{till}} < 0.003$, Eqn. 12, to fine-grained clay-rich till, $De^{\mathrm{s}}_{\mathrm{till}} < 0.03$, Eqn. 13. A small Deborah number (<< 1) indicates that, relative to the time scale of the deformation of the grain skeleton structure, the pore water pressure equilibrates near-instantaneously. A small Deborah number thus implies that pore pressure reduction in the expanding pore spaces of a deforming granular bed, a process that could contribute to the strengthening of the bed, does not occur in the critical state. The finding is in agreement with prior experimental findings of rate-independence of shear strength in the critical state (e.g., N. R. Iverson et al., 1998; Tulaczyk et al., 2000a).

This insight differs from but does not disagree with N. R. Iverson (2010), because N. R. Iverson (2010) discusses bed strengthening in the pre-critical state as a result of pore pressure reduction during episodes of dilation with incipient slip phases. There are two key differences between our calculations and N. R. Iverson (2010): the fact that we are considering the critical state whereas N. R. Iverson (2010) considers the transient dynamics, and the length scale over which spatial equilibration of pore pressure is assumed to occur. To clarify, we use the term "transient" with respect to the granular mechanics to identify the relatively short temporal period after the onset of granular motion during which the porosity of the granular medium changes until it reaches an approximately steady value. We do not exclude the possibility that other physical processes, such as water fluxes, exhibit time-dependent behavior.

N. R. Iverson (2010) considers the transient phase where sediment, initially in its consolidated state, dilates uniformly across the shear zone thickness. During such uniform dilation, pore pressure equilibration requires that pore water be transported into the expanding pore spaces from across the boundaries of the shear zone. Our analysis, on the other hand, focuses on a deforming till layer already at the critical state where the porosity fluctuates around a mean value. Under these conditions, pore pressure equilibration is more efficient than in the transient phase, since water may be transported to expanding pore spaces from neighboring pore spaces, leading to a relatively low Deborah number.

More broadly, estimation of the Deborah number sheds light on how pore pressure fluctuation can facilitate rate dependence in bed strength. Prior studies have suggested that pore pressure fluctuation can facilitate rate dependence in bed strength, where pore pressure reduction in expanding pore spaces can increase the effective normal stresses and shear resistance, and inversely, pore pressure increase in contracting pore spaces can enhance grain sliding through reduced normal stresses and friction (R. M. Iverson & Lahusen, 1989; R. M. Iverson et al., 2000; R. M. Iverson, 2005). In particular, the prior studies estimate the Deborah number for sedimentary stacks undergoing landslides to quantify the potential rate dependence in bed strength (R. M. Iverson et al., 2000; R. M. Iverson, 2005). Our estimate of a low Deborah number for subglacial till highlights that such rate dependence in bed strength resulting from pore pressure fluctuation at critical state is negligible.

Overall, a subglacial system being in the low Deborah number regime suggests that the pore fluid flow does not play a notable role in the dynamics of the bed during quasi-steady deformation. Aside from rate independence in till strength, rapid pore pressure equilibration at critical states ensures that pore pressure within the till is approximately independent of shear-induced changes in the grain skeleton structure. As a result, the pore pressure at the critical state is governed purely by hydrostatic pressure and the pressure gradients imposed by external hydrological systems near the subglacial interface.

5 Conclusion

Temperate granular beds are highly dynamic subglacial environments. The motion of the overlying ice shears the subglacial till, and the corresponding deformation alters the hydrological system at the ice-till interface. The goal of this study is to advance our process-based understanding of how the porosity of a subglacial granular bed is affected by laterally varying shear stresses. We represent the dynamics of shear deformation of till by using a three-dimensional discrete element model. Our results show that shear deformation creates zones of elevated porosity within the bed, even in the pseudo-static regime. Variability in basal speeds at the ice-bed interface elevates porosities in relatively narrow zones, and may facilitate the formation of canal-like hydrological structures through plastic failure. Porosity increases with local inertia number, the non-dimensional shear strain rate, but there is spatial variability in porosity at any given local inertia number. Shear deformation not only alters the porosity but also induces changes in the pore water pressure by altering the sizes of the pore spaces. For subglacial till at critical state, however, pore pressure equilibrates near-instantaneously relative to the time scale of grain skeleton deformation, inhibiting local strengthening or weakening behavior for the bed.

Acknowledgments

We thank Alejandro Cabrales-Vargas for performing initial DEM simulations. We thank Ed Bueler, Eric Dunham, and Lucas Zoet for fruitful conversations about our study. We also thank the three anonymous reviewers for providing valuable comments and critiques on our work.

This research was supported by the National Science Foundation through the Office of Polar Programs awards PLR-1341499 and PLR-1744758 and by the U.S. Army Research Laboratory under grant W911NF-12-R0012-04. This research used the XStream computational resource, supported by the National Science Foundation Major Research Instrumentation program (ACI-1429830). IK was supported by the Hewlett Family through the Stanford Graduate Fellowship. AD was funded by PLR-1744758 and the European Union's Horizon 2020 research and innovation programme under the Marie Skłodowska-Curie grant agreement No 897967.

Author Contributions: IK ran the simulations, prepared the figures, and wrote the majority of the manuscript. AD co-designed the simulations, co-advised IK, and developed the numerical code used. LG contributed to simulation design and interpretation. JS conceptualized the study, advised IK and AD, and contributed to simulation design and interpretation. All authors provided input on the manuscript text and figures.

The authors declare no conflict of interest with respect to the results of this paper.

Code availability: The DEM code *Sphere* is maintained at `https://src.adamsgaard.dk/sphere/`. The simulation outputs and visualization code used in our study are permanently archived at `https://doi.org/10.5281/zenodo.5541408`.

References

Aharonov, E., & Sparks, D. (2002). Shear profiles and localization in simulations of granular materials. *Physical Review E - Statistical Physics, Plasmas, Fluids, and Related Interdisciplinary Topics*, *65*(5), 12. doi: 10.1103/PhysRevE.65.051302

Alley, R., Blankenship, D., Bentley, C., & Rooney, S. (1987). Till beneath ice stream B: 3. Till deformation: evidence and implications. *Journal of Geophysical Research: Solid Earth*, *92*(B9), 8921–8929. doi: 10.1029/JB092iB09p08921

Amarsid, L., Delenne, J.-Y., Mutabaruka, P., Monerie, Y., Perales, F., & Radjai, F. (2017, 7). Viscoinertial regime of immersed granular flows. *Phys. Rev. E*, *96*(1), 12901. doi: 10.1103/PhysRevE.96.012901

Azéma, E., & Radjaï, F. (2014, 2). Internal structure of inertial granular flows. *Physical Review Letters*, *112*(7), 78001. doi: 10.1103/PhysRevLett.112.078001

Baumgarten, A. S., & Kamrin, K. (2019). A general fluidsediment mixture model and constitutive theory validated in many flow regimes. *Journal of Fluid Mechanics*, *861*, 721–764. doi: DOI:10.1017/jfm.2018.914

Benn, D. I., & Owen, L. A. (2002). Himalayan glacial sedimentary environments: a framework for reconstructing and dating the former extent of glaciers in high mountains. *Quaternary International*, *97-98*, 3–25. doi: https://doi.org/10.1016/S1040-6182(02)00048-4

Blankenship, D. D., Bentley, C. R., Rooney, S. T., & Alley, R. B. (1986). Seismic measurements reveal a saturated porous layer beneath an active Antarctic ice stream. *Nature*, *322*(6074), 54–57. doi: 10.1038/322054a0

Bougamont, M., Price, S., Christoffersen, P., & Payne, A. J. (2011, 12). Dynamic patterns of ice stream flow in a 3-D higher-order ice sheet model with plastic bed and simplified hydrology. *Journal of Geophysical Research: Earth Surface*, *116*(F4). doi: https://doi.org/10.1029/2011JF002025

Boulton, G. S., Dobbie, K. E., & Zatsepin, S. (2001). Sediment deformation beneath glaciers and its coupling to the subglacial hydraulic system. *Quaternary International*, *86*(1), 3–28. doi: 10.1016/S1040-6182(01)00048-9

Burman, B. C., Cundall, P. A., & Strack, O. D. (1980). A discrete numerical model for granular assemblies. *Geotechnique*, *30*(3), 331–336. doi: 10.1680/geot.1980.30.3.331

Carman, P. C. (1937). Fluid flow through granular beds. *Trans. Inst. Chem. Eng.*, *15*, 150–166.

Christianson, K., Peters, L. E., Alley, R. B., Anandakrishnan, S., Jacobel, R. W., Riverman, K. L., ... Keisling, B. A. (2014). Dilatant till facilitates ice-stream flow in northeast Greenland. *Earth and Planetary Science Letters*, *401*, 57–69. doi: https://doi.org/10.1016/j.epsl.2014.05.060

Clarke, G. K. (2005, 9). Subglacial processes. *Annual Review of Earth and Planetary Sciences*, *33*(1), 247–276. doi: 10.1146/annurev.earth.33.092203.122621

Costa, A. (2006, 1). Permeability-porosity relationship: A reexamination of the Kozeny-Carman equation based on a fractal pore-space geometry assumption. *Geophysical Research Letters*, *33*(2). doi: https://doi.org/10.1029/2005GL025134

Crawford, B. R., Faulkner, D. R., & Rutter, E. H. (2008). Strength, porosity, and permeability development during hydrostatic and shear loading of synthetic quartz-clay fault gouge. *Journal of Geophysical Research: Solid Earth*, *113*(3). doi: 10.1029/2006JB004634

Crawford, B. R., Myers, R., Woronow, A., Faulkner, D. R., & Rutter, E. H. (2002). Porosity-permeability relationships in clay-bearing fault gouge: Presented at the Society of Petroleum Engineers/International Society of Rock Mechanics, Rock Mechanics Conference, Irving, Texas, October 20-23,. *Spe/Isrm 78214*, 13p.

Cuffey, K. M., & Paterson, W. S. B. (2012). *The physics of glaciers.* Amsterdam [etc.]: Butterworth-Heinemann/Elsevier.

da Cruz, F., Emam, S., Prochnow, M., Roux, J., & Chevoir, F. (2005). Rheophysics of dense granular materials: Discrete simulation of plane shear flows. *Phys. Rev. E*, *72*(2). doi: 10.1103/physreve.72.021309

Damsgaard, A., Egholm, D. L., Beem, L. H., Tulaczyk, S., Larsen, N. K., Piotrowski, J. A., & Siegfried, M. R. (2016). Ice flow dynamics forced by water pressure variations in subglacial granular beds. *Geophysical Research Letters*, *43*(23), 165–12. doi: 10.1002/2016GL071579

Damsgaard, A., Egholm, D. L., Piotrowski, J. A., Tulaczyk, S., Larsen, N. K., & Brædstrup, C. F. (2015). A new methodology to simulate subglacial deformation of water-saturated granular material. *The Cryosphere*, *9*(6), 2183–2200. doi: 10.5194/tc-9-2183-2015

Damsgaard, A., Egholm, D. L., Piotrowski, J. A., Tulaczyk, S., Larsen, N. K., & Tylmann, K. (2013, 12). Discrete element modeling of subglacial sediment deformation. *Journal of Geophysical Research: Earth Surface*, *118*(4), 2230–2242. doi: 10.1002/2013JF002830

Damsgaard, A., Goren, L., & Suckale, J. (2020). Water pressure fluctuations control variability in sediment flux and slip dynamics beneath glaciers and ice streams. *Communications Earth & Environment*, *1*(1). doi: 10.1038/s43247-020-00074-7

Damsgaard, A., Suckale, J., Piotrowski, J. A., Houssais, M., Siegfried, M. R., & Fricker, H. A. (2017). Sediment behavior controls equilibrium width of subglacial channels. *Journal of Glaciology*, *63*(242), 1034–1048.
Engelhardt, H., & Kamb, B. (1997). Basal hydraulic system of a West Antarctic ice stream: constraints from borehole observations. *Journal of Glaciology*, *43*(144), 207–230.
Engelhardt, H., & Kamb, B. (1998). Basal sliding of Ice Stream B, West Antarctica. *Journal of Glaciology*, *44*(147), 223?230. doi: 10.3189/S0022143000002562
Ertaş, D., & Halsey, T. C. (2002). Granular gravitational collapse and chute flow. *Europhysics Letters (EPL)*, *60*(6), 931–937. doi: 10.1209/epl/i2002-00307-8
Evans, D., Phillips, E., Hiemstra, J., & Auton, C. (2006). Subglacial till: formation, sedimentary characteristics and classification. *Earth-Science Reviews*, *78*(1-2), 115–176.
Fischer, U. H., & Clarke, G. K. C. (2001). Review of subglacial hydro-mechanical coupling: Trapridge Glacier, Yukon Territory, Canada. *Quaternary International*, *86*(1), 29–43. doi: https://doi.org/10.1016/S1040-6182(01)00049-0
Flowers, G. E. (2015). Modelling water flow under glaciers and ice sheets. *Proceedings of the Royal Society of London A: Mathematical, Physical and Engineering Sciences*, *471*(2176). doi: 10.1098/rspa.2014.0907
Gaume, J., Chambon, G., & Naaim, M. (2011, 11). Quasistatic to inertial transition in granular materials and the role of fluctuations. *Physical Review E*, *84*(5), 51304. doi: 10.1103/PhysRevE.84.051304
Goren, L., Aharonov, E., Sparks, D., & Toussaint, R. (2010, 9). Pore pressure evolution in deforming granular material: A general formulation and the infinitely stiff approximation. *Journal of Geophysical Research: Solid Earth*, *115*(B9). doi: 10.1029/2009JB007191
Goren, L., Aharonov, E., Sparks, D., & Toussaint, R. (2011). The Mechanical Coupling of Fluid-Filled Granular Material Under Shear. *Pure and Applied Geophysics*, *168*(12), 2289–2323. doi: 10.1007/s00024-011-0320-4
Haseloff, M., Schoof, C., & Gagliardini, O. (2018, 8). The role of subtemperate slip in thermally driven ice stream margin migration. *The Cryosphere*, *12*(8), 2545–2568. doi: 10.5194/tc-12-2545-2018
Henann, D. L., & Kamrin, K. (2013). A predictive, size-dependent continuum model for dense granular flows. *Proceedings of the National Academy of Sciences*, *110*(17), 6730–6735. doi: 10.1073/pnas.1219153110
Hewitt, I. J. (2011). Modelling distributed and channelized subglacial drainage: the spacing of channels. *Journal of Glaciology*, *57*(202), 302–314.
Hewitt, I. J., Schoof, C., & Werder, M. A. (2012a). Flotation and free surface flow in a model for subglacial drainage. Part 2. Channel flow. *Journal of Fluid Mechanics*, *702*, 157–187. doi: 10.1017/jfm.2012.166
Hewitt, I. J., Schoof, C., & Werder, M. A. (2012b). Flotation and free surface flow in a model for subglacial drainage. Part 2. Channel flow. *Journal of Fluid Mechanics*, *702*, 157–187.
Hooke, R., & Iverson, N. R. (1995). Grain-size distribution in deforming subglacial tills: role of grain fracture. *Geology*, *23*(1), 57–60.
Houssais, M., Ortiz, C. P., Durian, D. J., & Jerolmack, D. J. (2015, 3). Onset of sediment transport is a continuous transition driven by fluid shear and granular creep. *Nature Communications*, *6*(6527), 6527. doi: 10.1038/ncomms7527
Iverson, N. R. (2010). Shear resistance and continuity of subglacial till: hydrology rules. *Journal of Glaciology*, *56*(200), 1104–1114.
Iverson, N. R., Cohen, D., Hooyer, T. S., Fischer, U. H., Jackson, M., Moore, P. L., ... Kohler, J. (2003, 7). Effects of Basal Debris on Glacier Flow. *Science*, *301*(5629), 81 LP - 84. doi: 10.1126/science.1083086
Iverson, N. R., & Hooyer, T. S. (2004, 12). Estimating the sliding velocity of a Pleistocene ice sheet from plowing structures in the geologic record. *Journal of*

Geophysical Research: Earth Surface, *109*(F4). doi: 10.1029/2004JF000132
Iverson, N. R., Hooyer, T. S., & Baker, R. W. (1998). Ring-shear studies of till deformation: Coulomb-plastic behavior and distributed strain in glacier beds. *Journal of Glaciology*, *44*(148), 634–642.
Iverson, N. R., Hooyer, T. S., Fischer, U. H., Cohen, D., Moore, P. L., Jackson, M., ... Kohler, J. (2007). Soft-bed experiments beneath Engabreen, Norway: Regelation, infiltration, basal slip and bed deformation. *Journal of Glaciology*, *53*(182), 323–340. doi: 10.3189/002214307783258431
Iverson, N. R., & Zoet, L. K. (2015). Experiments on the dynamics and sedimentary products of glacier slip. *Geomorphology*, *244*, 121–134. doi: https://doi.org/10.1016/j.geomorph.2015.03.027
Iverson, R. M. (2005). Regulation of landslide motion by dilatancy and pore pressure feedback. *Journal of Geophysical Research: Earth Surface*, *110*(2), 1–16. doi: 10.1029/2004JF000268
Iverson, R. M., & Lahusen, R. G. (1989). Dynamic pore-pressure fluctuations in rapidly shearing granular materials. *Science*, *246*(4931), 796–799. doi: 10.1126/science.246.4931.796
Iverson, R. M., Reid, M. E., Iverson, N. R., LaHusen, R. G., Logan, M., Mann, J. E., & Brien, D. L. (2000). Acute sensitivity of landslide rates to initial soil porosity. *Science*, *290*(5491), 513–516. doi: 10.1126/science.290.5491.513
Jacobson, H. P., & Raymond, C. F. (1998, 6). Thermal effects on the location of ice stream margins. *Journal of Geophysical Research: Solid Earth*, *103*(6), 12111–12122. doi: 10.1029/98jb00574
Jenkins, J. T., & Savage, S. B. (1983). A theory for the rapid flow of identical, smooth, nearly elastic, spherical particles. *Journal of Fluid Mechanics*, *130*, 187–202. doi: DOI:10.1017/S0022112083001044
Jop, P. (2008, 3). Hydrodynamic modeling of granular flows in a modified Couette cell. *Physical Review E*, *77*(3), 32301. doi: 10.1103/PhysRevE.77.032301
Jop, P., Forterre, Y., & Pouliquen, O. (2006). A constitutive law for dense granular flows. *Nature*, *441*(7094), 727–730. doi: 10.1038/nature04801
Kasmalkar, I., Mantelli, E., & Suckale, J. (2019, 8). Spatial heterogeneity in subglacial drainage driven by till erosion. *Proceedings of the Royal Society A: Mathematical, Physical and Engineering Sciences*. doi: 10.1098/rspa.2019.0259
Kim, S., & Kamrin, K. (2020). Power-Law Scaling in Granular Rheology across Flow Geometries. *Physical Review Letters*, *125*(8), 88002. doi: 10.1103/PhysRevLett.125.088002
Koval, G., Roux, J. N., Corfdir, A., & Chevoir, F. (2009, 2). Annular shear of cohesionless granular materials: From the inertial to quasistatic regime. *Physical Review E - Statistical, Nonlinear, and Soft Matter Physics*, *79*(2), 21306. doi: 10.1103/PhysRevE.79.021306
Kozeny, J. (1927). Uber kapillare leitung der wasser in boden. *Royal Academy of Science, Vienna, Proc. Class I*, *136*, 271–306.
Kruggel-Emden, H., Simsek, E., Rickelt, S., Wirtz, S., & Scherer, V. (2007). Review and extension of normal force models for the Discrete Element Method. *Powder Technology*, *171*(3), 157–173. doi: 10.1016/j.powtec.2006.10.004
Kruggel-Emden, H., Wirtz, S., & Scherer, V. (2008). A study on tangential force laws applicable to the discrete element method (DEM) for materials with viscoelastic or plastic behavior. *Chemical Engineering Science*, *63*(6), 1523–1541. doi: 10.1016/j.ces.2007.11.025
Leeman, J. R., Valdez, R. D., Alley, R. B., Anandakrishnan, S., & Saffer, D. M. (2016, 7). Mechanical and hydrologic properties of Whillans Ice Stream till: Implications for basal strength and stick-slip failure. *Journal of Geophysical Research: Earth Surface*, *121*(7), 1295–1309. doi: 10.1002/2016JF003863
Lindeque, A., Gohl, K., Wobbe, F., & Uenzelmann-Neben, G. (2016, 10). Preglacial to glacial sediment thickness grids for the Southern Pacific Margin of West Antarctica.

Geochemistry, Geophysics, Geosystems, *17*(10), 4276–4285. doi: 10.1002/2016GC006401

Lopera Perez, J. C., Kwok, C. Y., O'Sullivan, C., Huang, X., & Hanley, K. J. (2016). Assessing the quasi-static conditions for shearing in granular media within the critical state soil mechanics framework. *Soils and Foundations*, *56*(1), 152–159. doi: 10.1016/j.sandf.2016.01.013

Luding, S. (2008). Introduction to discrete element methods. Basic of contact force models and how to perform the micro-macro transition to continuum theory. *Revue européenne de génie civil*, *12*(7-8), 785–826. doi: 10.3166/ejece.12.785-826

Mair, D., Willis, I., Fischer, U. H., Hubbard, B., Nienow, P., & Hubbard, A. (2003). Hydrological controls on patterns of surface, internal and basal motion during three spring events: Haut Glacier dArolla, Switzerland. *Journal of Glaciology*, *49*(167), 555–567. doi: DOI:10.3189/172756503781830467

McNamara, S., Flekkøy, E. G., & Måløy, K. J. (2000, 4). Grains and gas flow: Molecular dynamics with hydrodynamic interactions. *Physical Review E - Statistical Physics, Plasmas, Fluids, and Related Interdisciplinary Topics*, *61*(4), 4054–4059. doi: 10.1103/PhysRevE.61.4054

MiDi, G. D. R. (2004). On dense granular flows. *The European Physical Journal E*, *14*(4), 341–365. doi: 10.1140/epje/i2003-10153-0

Moore, P. L., & Iverson, N. R. (2002). Slow episodic shear of granular materials regulated by dilatant strengthening. *Geology*, *30*(9), 843. doi: 10.1130/0091-7613(2002)030⟨0843:sesogm⟩2.0.co;2

Ng, F. S. (2000). Coupled ice–till deformation near subglacial channels and cavities. *Journal of Glaciology*, *46*(155), 580–598.

Orpe, A. V., & Khakhar, D. V. (2001, 8). Scaling relations for granular flow in quasi-two-dimensional rotating cylinders. *Physical Review E*, *64*(3), 31302. doi: 10.1103/PhysRevE.64.031302

Perol, T., Rice, J. R., Platt, J. D., & Suckale, J. (2015). Subglacial hydrology and ice stream margin locations. *Journal of Geophysical Research: Earth Surface*, *120*(7), 1352–1368.

Rathbun, A. P., Marone, C., Alley, R. B., & Anandakrishnan, S. (2008, 6). Laboratory study of the frictional rheology of sheared till. *Journal of Geophysical Research: Earth Surface*, *113*(F2). doi: https://doi.org/10.1029/2007JF000815

Scheuchl, B., Mouginot, J., & Rignot, E. (2012). Ice velocity changes in the Ross and Ronne sectors observed using satellite radar data from 1997 and 2009. *Cryosphere*, *6*(5), 1019–1030. doi: 10.5194/tc-6-1019-2012

Schoof, C. (2004). On the mechanics of ice-stream shear margins. *Journal of Glaciology*, *50*(169), 208–218. doi: DOI:10.3189/172756504781830024

Silbert, L. E., Ertaş, D., Grest, G. S., Halsey, T. C., Levine, D., & Plimpton, S. J. (2001, 10). Granular flow down an inclined plane: Bagnold scaling and rheology. *Physical Review E - Statistical Physics, Plasmas, Fluids, and Related Interdisciplinary Topics*, *64*(5), 14. doi: 10.1103/PhysRevE.64.051302

Suckale, J., Platt, J. D., Perol, T., & Rice, J. R. (2014, 5). Deformation-induced melting in the margins of the West Antarctic ice streams. *J. Geophys. Res. Earth Surf.*, *119*(5), 1004–1025. doi: 10.1002/2013jf003008

Truffer, M., & Harrison, W. D. (2006). In situ measurements of till deformation and water pressure. *Journal of Glaciology*, *52*(177), 175–182. doi: DOI:10.3189/172756506781828700

Truffer, M., Harrison, W. D., & Echelmeyer, K. A. (2000). Glacier motion dominated by processes deep in underlying till. *Journal of Glaciology*, *46*(153), 213–221. doi: 10.3189/172756500781832909

Tulaczyk, S., Kamb, B., Scherer, R. P., & Engelhardt, H. F. (1998). Sedimentary processes at the base of a West Antarctic ice stream; constraints from textural and compositional properties of subglacial debris. *Journal of Sedimentary Research*, *68*(3), 487–496.

Tulaczyk, S., Kamb, W. B., & Engelhardt, H. F. (2000a). Basal mechanics of ice stream B, West Antarctica: 1. Till mechanics. *Journal of Geophysical Research: Solid Earth*, *105*(B1), 463–481.
Tulaczyk, S., Kamb, W. B., & Engelhardt, H. F. (2000b). Basal mechanics of ice stream B, West Antarctica: 2. Undrained plastic bed model. *Journal of Geophysical Research: Solid Earth*, *105*(B1), 463–481.
Walder, J. S. (1982). Stability of sheet flow of water beneath temperate glaciers and implications for glacier surging. *Journal of Glaciology*, *28*(99), 273–293.
Walder, J. S., & Fowler, A. (1994). Channelized subglacial drainage over a deformable bed. *Journal of Glaciology*, *40*(134), 3–15.
Werder, M. A., Hewitt, I. J., Schoof, C. G., & Flowers, G. E. (2013). Modeling channelized and distributed subglacial drainage in two dimensions. *Journal of Geophysical Research: Earth Surface*, *118*(4), 2140–2158.
Zoet, L. K., & Iverson, N. R. (2020, 4). A slip law for glaciers on deformable beds. *Science*, *368*(6486), 76 LP - 78. doi: 10.1126/science.aaz1183

Appendix A Low Deborah number systems have approximately hydrostatic pressure conditions

In Section 3.1, we estimate that the subglacial systems considered in this study have low Deborah numbers. As a result, spatial equilibration of pore pressure within the bed happens substantially faster than shear-induced grain rearrangement, suggesting that the pore pressure remains approximately hydrostatic in the absence of external pressure gradients, and that the grain-fluid interactions could be well approximated by Eqn. (4). To test the assumption of hydrostatic pressure conditions, we run DEM simulations using *Sphere* (Damsgaard et al., 2013, 2015) with coupled granular deformation and pore fluid flow.

To perform the coupled DEM simulations, we divide the domain of the simulation into a collection of $10 \times 10 \times 10$ cubic elements, as shown in Fig. 2. We assume that the elements are representative volumes where Darcy's law holds. Darcy's law is given by,

$$\mathbf{q} = -\frac{k}{\eta}\nabla p, \tag{A1}$$

where $\mathbf{q}$ [m/s] is the volumetric flux rate per unit area, k [m^2] is the permeability, and η [Pa s] is the dynamic fluid viscosity. The grain-fluid coupling is achieved by solving Eqn. 7 that describes the cell-scale pore fluid pressure evolution over the grid defined by the elements, and using the time and space dependent dynamic pore pressure gradients to evaluate the full form of the grain-fluid interaction term in Eqn. (3).

We assume a constant zero pressure at the top boundary, no-flow condition at the bottom and lateral boundaries, and periodicity at the x-boundaries. The full details of the coupled grain motion and fluid flow solver are provided in Damsgaard et al. (2015).

We run simulations for the laterally varying shear configuration with coupled fluid flow and plot the fluid pressure profile averaged over the last 2 seconds of the simulation in Fig. A1. The figure shows approximately hydrostatic profiles, which supports our result in Section 3.1.

Appendix B Simple shear simulations over a range of effective normal stresses

In Fig. B1, we plot the grain velocity, shear strain rate, and porosity for the simple shear configuration with $\sigma = \{10, 20, 30, 40, 50, 60, 70, 80\}$ kPa. The figure suggests that the thicknesses of the shear zone and the zone of elevated porosity increase with effective normal stress σ for $\sigma < 60$ kPa, and decrease slightly beyond 60 kPa.

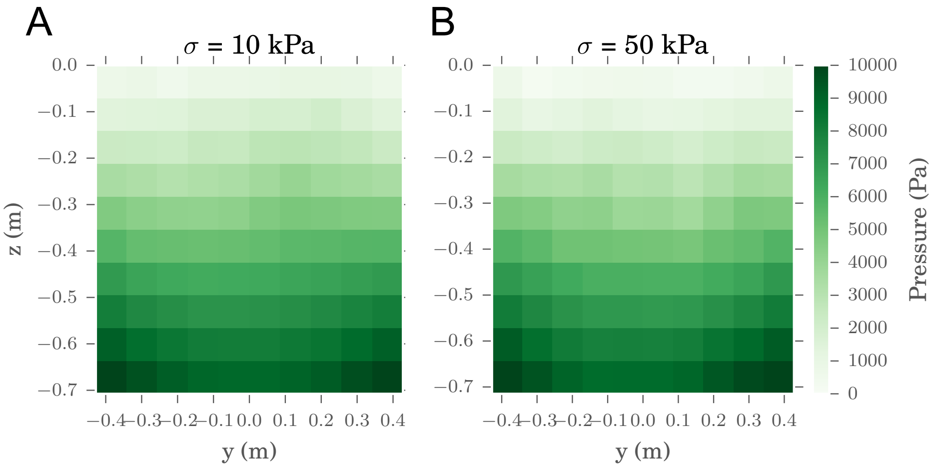

Figure A1. Pore pressure profile at the end of the lateral shear configuration, for effective normal stresses $\sigma = 10, 50\,\text{kPa}$.

Appendix C Bed thickness does not affect grain velocities

A relatively small bed thickness in the DEM may introduce boundary effects into our simulations. To test whether bed thickness affects grain motion, we conduct simple shear DEM simulations with thicker granular beds in Fig. C1. We choose the granular bed to have twice the thickness as that of Fig. 2, and with twice number of grains ($n = 20000$). Our results show that grain velocity profiles do not change with the thickness of the bed, suggesting that the vertical boundaries do not introduce any noticeable effects into grain motion.

Appendix D Fixed lateral boundaries in the model do not affect the porosity or shear strain rate

In the DEM, we impose fixed, frictionless lateral boundaries to constrain the granular bed (Fig. 1A). To test whether the lateral boundaries introduce boundary effects that distort the distribution of porosity and shear strain rate within the bed, we conduct a sensitivity test where we simulate a granular beds with twice the width as in Fig. 5 and twice the number of grains ($n = 20000$). We perform simulations with the laterally varying shear to identify any potential boundary effects on either the lateral or vertical components of the shear strain rates.

The results for effective normal stresses $\sigma = 10$kPa (Fig. D1) and $\sigma = 50$kPa (Fig. D2) show approximately similar distributions of shear strain rate and porosity as compared to Figs. 5 and 6. The porosity values near the center of the shear interface are slightly higher for the wider bed than for the regular bed (Fig. 5), but the difference is less than 5% in magnitude. Overall, our results suggest that porosity and shear strain rates do not change notably with changes in the width of the domain.

Appendix E Using granular temperature to estimate porosity

Prior studies suggest that the dynamics of homogeneous shear flows are well captured by a single parameter, the inertia number (MiDi, 2004; da Cruz et al., 2005; Henann & Kamrin, 2013; Azéma & Radjaï, 2014). However, the introduction of laterally varying shear, or even gravity, adds non-local behavior at scales smaller than the domain, thus

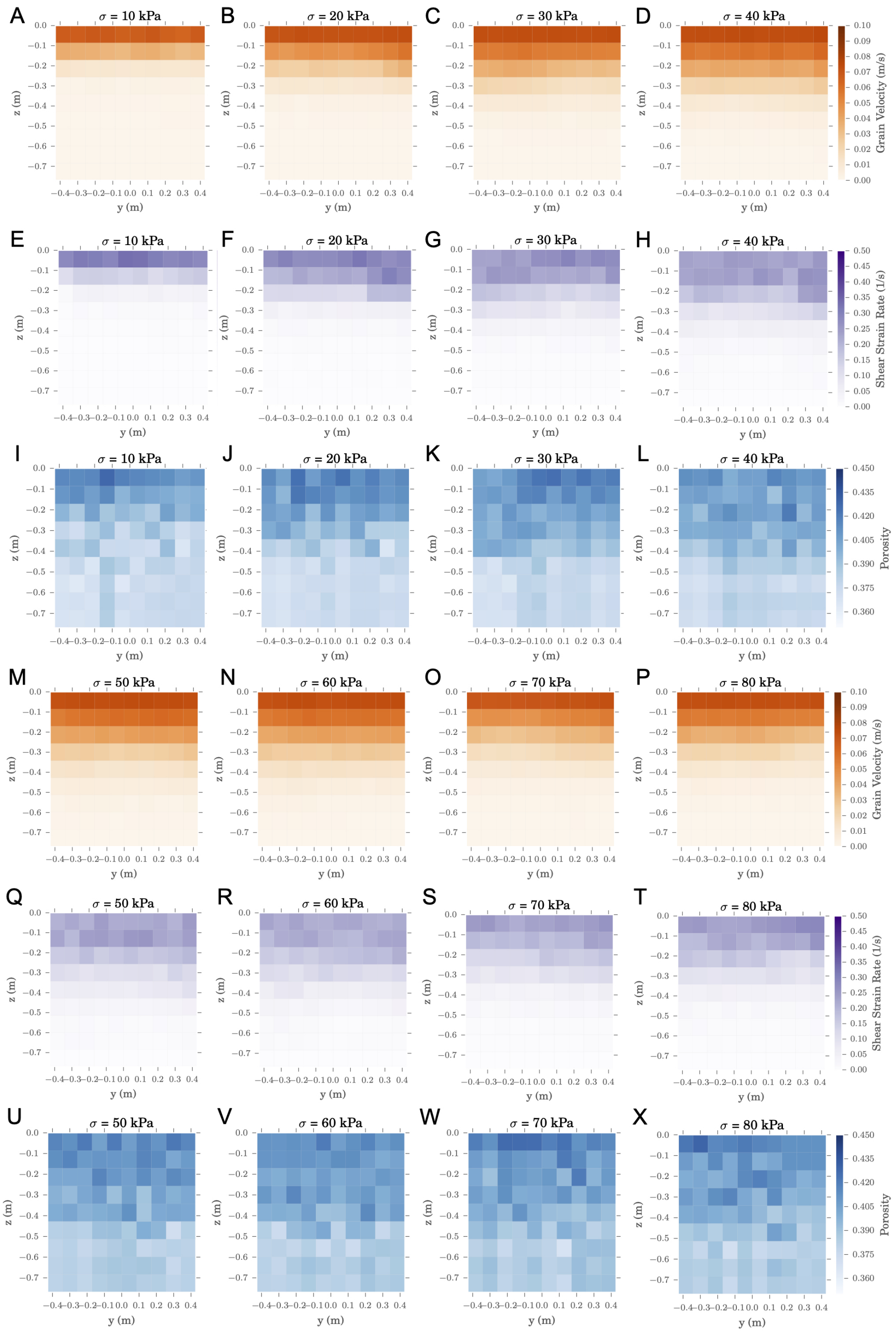

Figure B1. Simulation results for the simple shear configuration (Fig. 1B) for effective normal stress $\sigma = \{10, 20, 30, 40, 50, 60, 70, 80\}$ kPa.

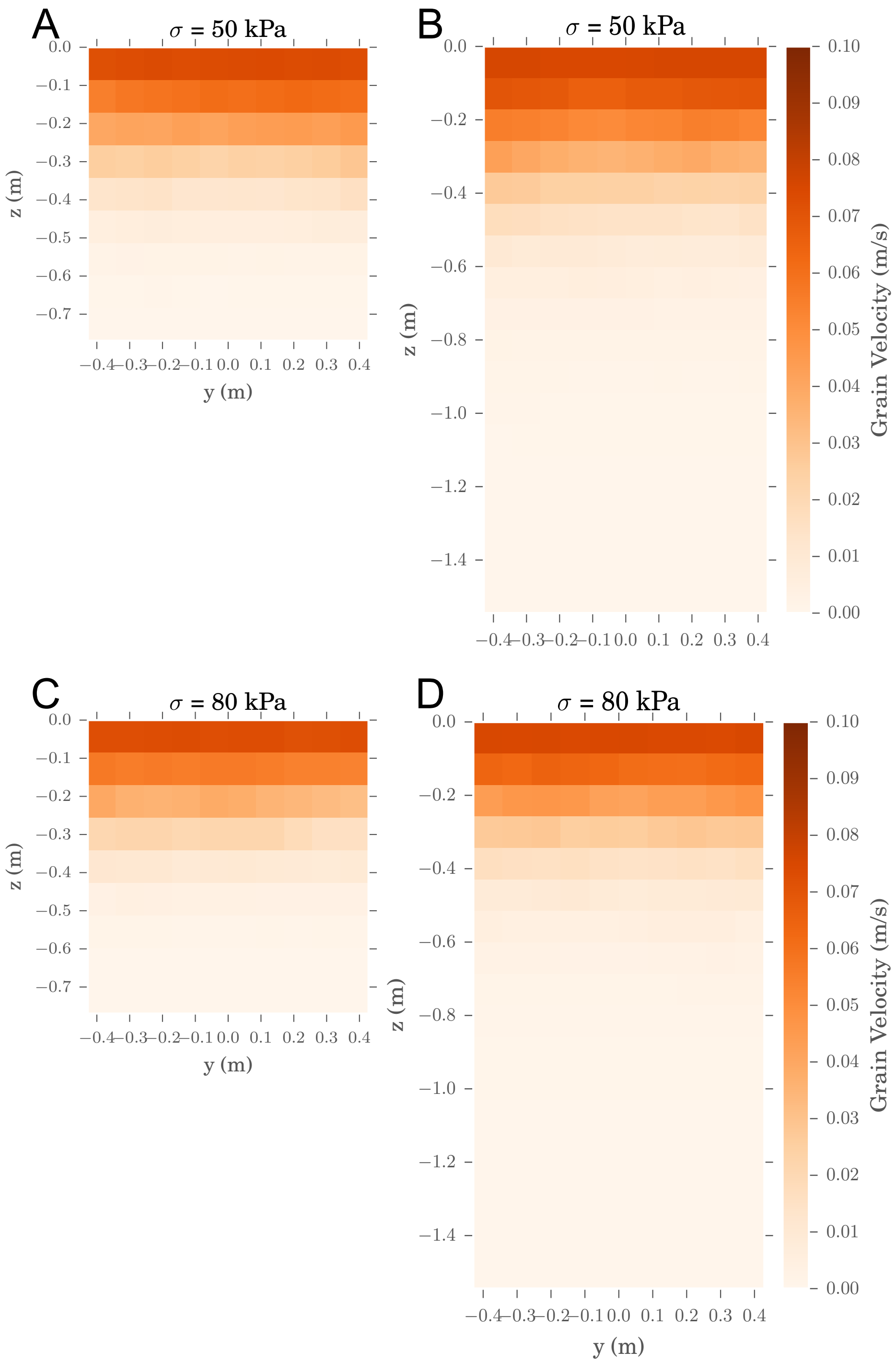

Figure C1. Grain velocities for the simple shear configuration, averaged along the x-direction, for different bed thicknesses. (A) Normal domain thickness, $\sigma = 50\,\text{kPa}$. (B) Extended domain thickness, $\sigma = 50\,\text{kPa}$. (C) Normal domain thickness, $\sigma = 80\,\text{kPa}$. (D) Extended domain thickness, $\sigma = 80\,\text{kPa}$.

requiring an additional constraining variable. The study by Kim and Kamrin (2020)

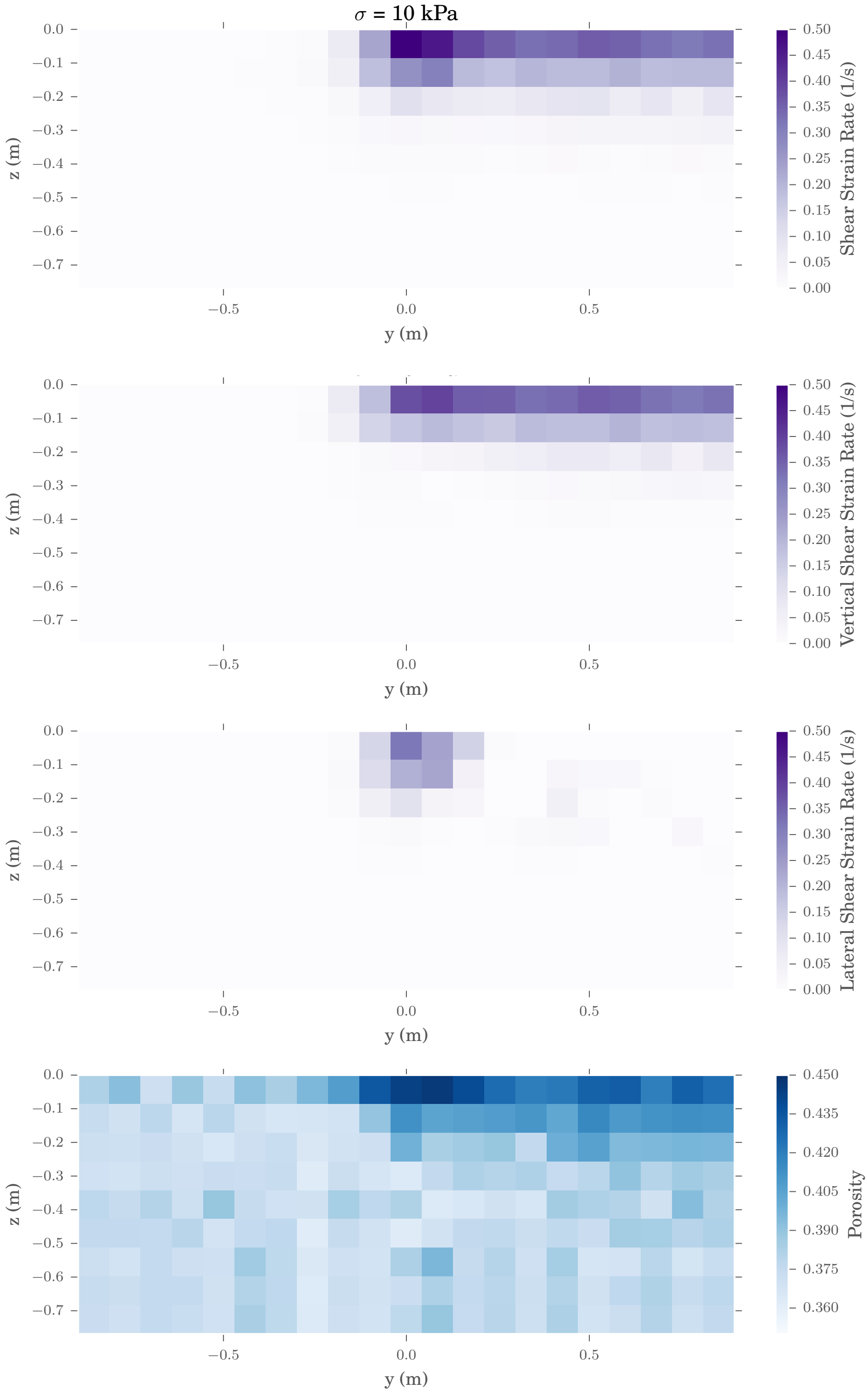

Figure D1. Grain velocities for the laterally varying shear configuration with $\sigma = 10$kPa, averaged along the x-direction, for a relatively wide bed. (A) The shear strain rate. (B) The vertical component of the shear strain rate. (C) The lateral component of the shear strain rate. (D) Porosity.

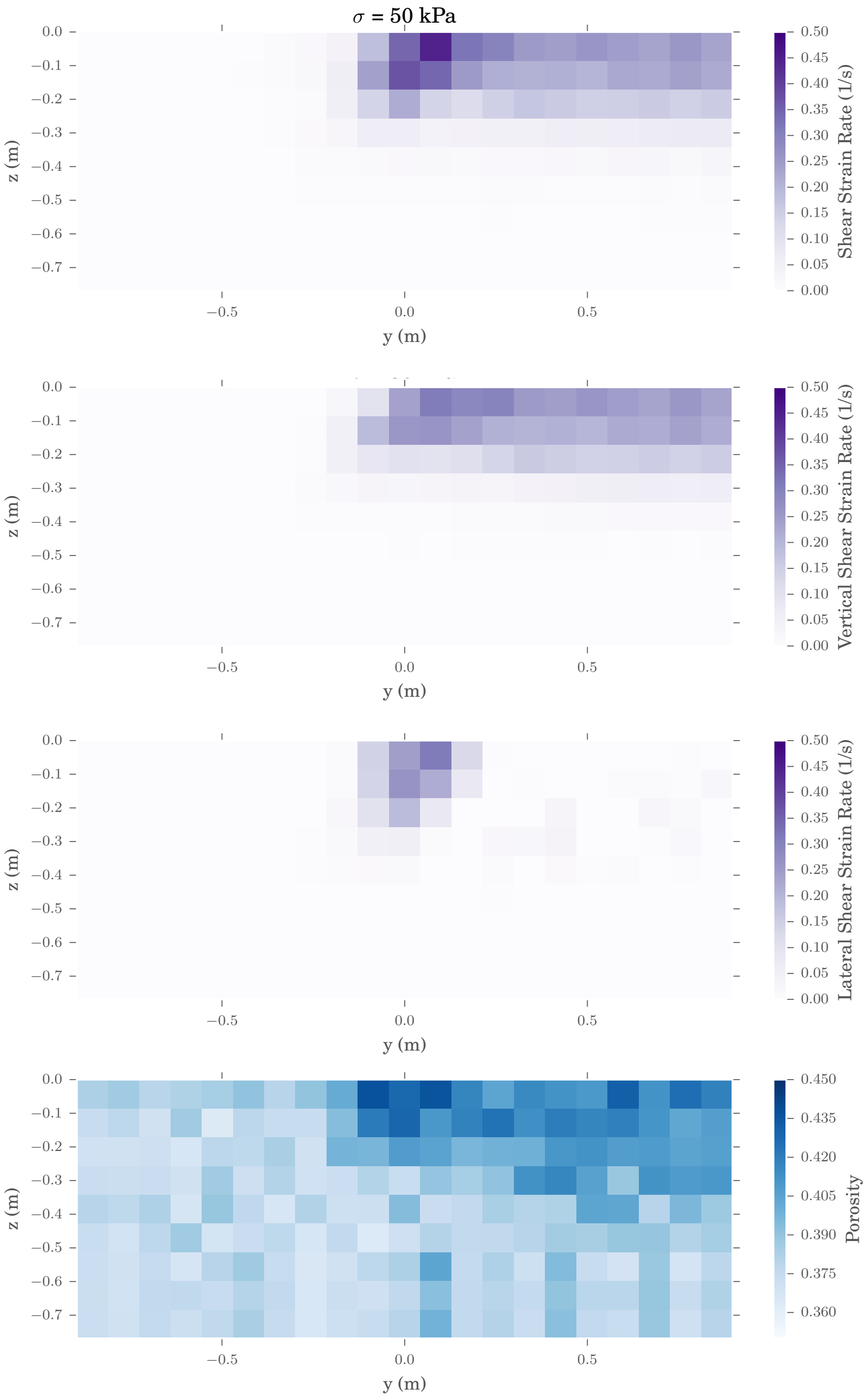

Figure D2. Grain velocities for the laterally varying shear configuration with $\sigma = 50$kPa, averaged along the x-direction, for a relatively wide bed. (A) The shear strain rate. (B) The vertical component of the shear strain rate. (C) The lateral component of the shear strain rate. (D) Porosity.

suggests one such potential candidate variable: granular temperature, namely, the

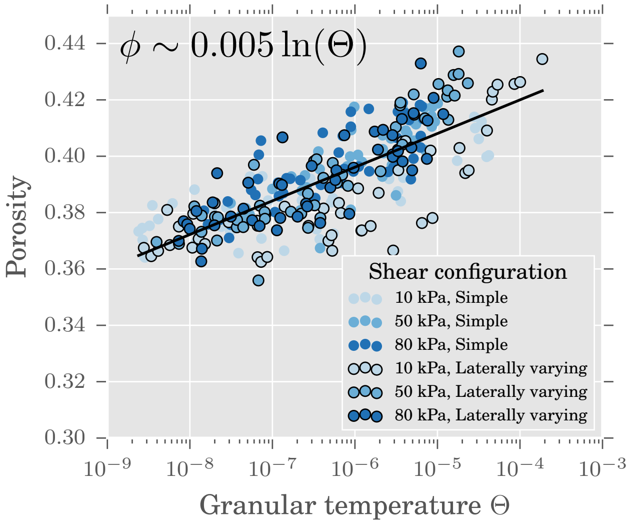

Figure E1. Porosity ϕ and granular temperature Θ for the cells of six DEM simulations superimposed together. The simulations include the simple and laterally varying shear configurations for effective normal stresses 10, 50, and 80kPa respectively. The trendline, shown in black, is calculated with ordinary least squares linear regression in semi-log scale. Data associated with boundary cells have been removed to avoid boundary effects.

non-dimensionalized fluctuations of grain velocity,

$$\Theta = \frac{\delta v^2}{\sigma/\rho_g}, \tag{E1}$$

where δv^2 is the spatial variance of the grain velocities.

Given our focus on understanding the evolution of porosity in deforming granular beds, we test the relationship between porosity and granular temperature. Fig. E1 shows a linear relationship between the porosity and the logarithm of the granular temperature across a range of simulations, including those with laterally varying shear. Our results are consistent with the kinetic theory pioneered by Jenkins and Savage (1983) which posits that porosity scales with the magnitude of grain velocity fluctuations.